An Eulerian crystal plasticity framework for modeling large anisotropic deformations in energetic materials under shocks

Sen, Oishik
Durate, Camilo A.
Rai, Nirmal Kumar
Koslowski, Marisol
Udaykumar, H.S.

To be published in: Journal of Applied Physics

DOI to publisher's version: 10.1063/5.0091911

Journal of Applied Physics

RESEARCH ARTICLE | NOVEMBER 09 2022

An Eulerian crystal plasticity framework for modeling large anisotropic deformations in energetic materials under shocks

Oishik Sen ; Camilo A. Duarte ; Nirmal Kumar Rai ; Marisol Koslowski ; H. S. Udaykumar

J. Appl. Phys. 132, 185902 (2022)
https://doi.org/10.1063/5.0091911

AIP Publishing

Journal of Applied Physics METHOD scitation.org/journal/jap

An Eulerian crystal plasticity framework for modeling large anisotropic deformations in energetic materials under shocks

Cite as: J. Appl. Phys. 132, 185902 (2022); doi: 10.1063/5.0091911
Submitted: 18 March 2022 · Accepted: 14 October 2022 ·
Published Online: 9 November 2022

Oishik Sen,[1] Camilo A. Duarte,[2] Nirmal Kumar Rai,[3] Marisol Koslowski,[2] and H. S. Udaykumar[1,a)]

AFFILIATIONS

[1]Department of Mechanical Engineering, The University of Iowa, Iowa City, Iowa 52242, USA
[2]Department of Mechanical Engineering, Purdue University, West Lafayette, Indiana 47907, USA
[3]Theoretical Division, Los Alamos National Laboratory, Los Alamos, New Mexico 87545, USA

[a)]**Author to whom correspondence should be addressed:** hs-kumar@uiowa.edu

ABSTRACT

This paper demonstrates a novel Eulerian computational framework for modeling anisotropic elastoplastic deformations of organic crystalline energetic materials (EM) under shocks. While Eulerian formulations are advantageous for handling large deformations, constitutive laws in such formulations have been limited to isotropic elastoplastic models, which may not fully capture the shock response of crystalline EM. The present Eulerian framework for high-strain rates, large deformation material dynamics of EM incorporates anisotropic isochoric elasticity via a hypo-elastic constitutive law and visco-plastic single-crystal models. The calculations are validated against atomistic calculations and experimental data and benchmarked against Lagrangian (finite element) crystal plasticity computations for shock-propagation in a monoclinic organic crystal, octahydro-1,3,5,7-tetranitro-1,3,5,7 tetrazocine (β-HMX). The Cauchy stress components and the resolved shear stresses calculated using the present Eulerian approach are shown to be in good agreement with the Lagrangian computations for different crystal orientations. The Eulerian framework is then used for computations of shock-induced inert void collapse in β-HMX to study the effects of crystal orientations on hotspot formation under different loading intensities. The computations show that the hotspot temperature distributions and the collapse profiles are sensitive to the crystal orientations at lower impact velocities (viz., 500 m/s); when the impact velocity is increased to 1000 m/s, the collapse is predominantly hydrodynamic and the role of anisotropy is modest. The present methodology will be useful to simulate energy localization in shocked porous energetic material microstructures and other situations where large deformations of single and polycrystals govern the thermomechanical response.

I. INTRODUCTION

Shock initiation of energetic materials (EMs) is a significant concern, both from the standpoint of safety and performance of these sensitive and hazardous materials. Initiation of EM occurs in the microstructure (i.e., at the meso-scale) at "hotspots." Such hotspots can arise due to inter- and intra-crystal void collapse,[1,2] shear band formation,[3] inter-crystal frictional interactions, and energy localization at defects and interfaces.[4] Meso-scale simulations of single crystals[3,5,6] and microstructures containing fields of crystals[7] have become increasingly important to understand, characterize, and predict the shock response, in particular, the shock sensitivity and advent of detonation in energetic materials. Accurately portraying the shock dynamics of EM demands both computational accuracy as well as physical fidelity in the modeling and simulation frameworks. Several methods and corresponding models have been explored in the literature to highlight the requirements for accurate numerical calculations[8,9] and material model representation[6,10] of EM at the meso-scale, i.e., in the microstructure. EM microstructures can vary depending on the application, typically consisting of a mixture of energetic crystals, binder materials, and inclusions. The crystals and defect structures (voids and interfaces) are morphologically complex, and they can dynamically evolve under shock loading. Large deformations and topological changes can present challenges to computational methods, such as Lagrangian finite element methods, which discretize the computational domain using boundary-fitted meshes. In recent years, Eulerian computational

approaches[8,9,11] using simple Cartesian, non-body-conforming meshes have been extensively used for meso-scale simulations of microstructures and their thermo-mechanical response to shock loading. However, Eulerian formulations have mainly been used in hydro-codes, which focused on accurate modeling of high volumetric compression of materials under shocks.[12] The material models in such cases have tended to be isotropic, with models for the deviatoric elastic and subsequent plastic responses that may not capture key aspects of the deformation processes in anisotropic materials. This work seeks to advance Eulerian material dynamics frameworks by more accurately representing material deformation through the incorporation of anisotropic single crystal plasticity models for EM.

High strain rate, high pressure and temperature, and extreme deformation of EM need to be modeled to understand and predict shock initiation. Organic crystals in high explosives (HEs) undergo large anisotropic deformations under shocks. For example, the widely used 1,3,5,7-tetranitro-1,3,5,7-tetrazocane (HMX) is a monoclinic crystal, while 1,3,5-triamino-2,4,6-trinitro benzene (popularly known as TATB) is a triclinic crystal; the dynamic response of these EMs is significantly affected by the direction of the loading with respect to crystalline slip planes.[13] Typical isotropic plasticity models cannot explicitly model the sensitivity of these materials for specific loading directions. Furthermore, they cannot directly incorporate the crucial sub-grid scale (SGS) dynamics of dislocation mobility, cross-slip, dislocation nucleation and annihilation, etc., that drives the plastic flow, especially in organic crystals under shocks.[14–17] Accurate modeling of the elastoplastic deformation of shocked EM is critical for predicting the shock sensitivity of these materials. Barton *et al.*[6] incorporated dislocation generation behind a shock wave via a thermal-activation based single-crystal plasticity model for β-HMX and observed the formation of shear-bands during shock-induced void-collapse of β-HMX. Austin *et al.*[3] used a similar model to perform reactive void-collapse computations of β-HMX and demonstrated the roles of shear-enabled micro-jetting and localization due to shear-bands in driving the deflagration front of β-HMX. Luscher *et al.*[10] developed a crystal plasticity model for α-RDX (cyclotrimethylene trinitramine) to incorporate dislocation multiplication on individual slip systems. Grilli and Koslowski[5] incorporated glide-based crystal plasticity models into continuum frameworks for meso-scale modeling of void-collapse in β-HMX and showed good agreement with void-collapse experiments and atomistic calculations.[18,19] These studies indicate that the micro-mechanics of EM crystals can significantly impact energy localization and therefore the initiation sensitivity of EM. Therefore, at least at low to moderate shock strengths, the anisotropic crystalline deformation processes must be captured in meso-scale simulations of EM microstructures.

Eulerian formulations offer advantages in modeling materials subject to extreme deformations under impact, shocks, and detonations, including topological changes such as collapse, spall, and fragmentation.[9,20–22] They typically employ regular Cartesian grids, where multiple materials are embedded and can flow through the grid during the deformation process. Since the grid points are not tied to the material, problems of extreme mesh deformation and mesh management are avoided. The simple topology of the mesh also facilitates the use of well-developed, high accuracy shock capturing schemes that produce non-oscillatory solutions under high strain rate, large deformation, and transient loading conditions.[23–25] Additionally, for materials undergoing chemical reactions, multi-species combustion and tracking of deflagration fronts are also relatively straightforward to implement in Eulerian mixture-based formulations.[25–27] The challenge in Eulerian models is in accurately representing the mechanics of elastoplastic deformation of solid materials. For example, Wilkins[28] incorporated plasticity into hydrocodes via the J2 flow theory and Drucker's postulate[29] in earlier works on modeling isochoric elastoplasticity in materials under shocks. Such isotropic elastoviscoplastic flow models have continued to be the norm in Eulerian[8,9,11,23] as well as ALE[2,3] codes applied to study the dynamics of EM. To date, the use of single crystal plasticity has been mostly limited to Lagrangian[5] or ALE formulations.[3] An exception in this regard is the earlier work by Cazacu and Ionescu[30] that demonstrated a computational framework for dynamic crystal plasticity using an Eulerian approach; however, the work was limited to incompressible materials, isotropic elasticity, and rigid plasticity. In a different application, Kratochvil *et al.*[31] advanced the Eulerian formulation by relaxing the assumption of rigid plasticity and incompressibility; however, they incorporated their formulation in an ALE framework for modeling the plastic response of materials under finite strains.

While these works on Eulerian crystal plasticity have been pursued for finite strains, to the authors' knowledge, there is no computational framework for modeling crystal plasticity in high strain-rate loading scenarios such as shocks and impacts. The work presented here seeks to develop an Eulerian model that takes advantage of the Cartesian grid, sharp interface, TVD-ENO shock capturing, and arbitrary deformation features[20,21,23,32,33] to simulate the collapse of voids in an organic energetic crystal, specifically HMX. While the baseline computational solver employed[1,20,21,23,32] has been extensively validated, the novel Eulerian approach for anisotropic crystal plasticity in this work needs to be validated and benchmarked to establish that the computed anisotropic deformation and stress fields are correctly represented in the presence of shock loading. This paper achieves this in the following ways:

1. Since Lagrangian models are traditionally employed for the simulation of anisotropic material dynamics simulations, they can serve as a benchmark for the current Eulerian modeling framework. In particular, the Lagrangian simulations can be employed to compare head-to-head the details of stresses developed in the material along different crystalline orientations; this would not be possible to do with experimental data. The Lagrangian model incorporates a glide-based model for describing the anisotropic plastic response of shocked β-HMX and solves the governing equations using the well-tested MOOSE finite element code. The Lagrangian model has previously been validated against both experimental void collapse results[18] as well as molecular dynamics (MD) computations.[19] The material model, including the equations of state, the elasticity constants, as well as the plasticity model in the Lagrangian computations in Refs. 18 and 19 are identical to the material model implemented in the present Eulerian approach. Therefore, for the purpose of benchmarking the Eulerian framework, we compare our results with the Lagrangian model for β-HMX.[18,19]

2. To closely follow the material modeling framework in previous studies on void collapse in β-HMX,[5,18,19] the present Eulerian representation uses an anisotropic hypo-elastic constitutive description for modeling the elastic response of the EM, while the plastic response is described using single crystal viscoplastic models.[5] Therefore, in addition to benchmarking against the Lagrangian calculations for the individual components of the stresses, the bulk response to shocks from Eulerian calculations is also validated against MD-derived[19] and experimentally measured material responses.[34]

The remainder of the paper is organized as follows. Section II provides details of the global conservation laws, which are solved in conjunction with the kinematic evolution equations to track the crystalline orientations. Section III presents the results of the calculations, where the Eulerian computations are compared rigorously against Lagrangian hyper-elastic computations for the monoclinic crystal β-HMX, for different loading directions. Section III B compares the shock Hugoniot obtained by using the Eulerian computations with MD Hugoniotstat data,[19] as well as with the experimental Hugoniot reported in Menikoff and Sewell.[34] The framework is then used in Sec. III C to simulate shock-induced void collapse of β-HMX under different loading intensities to study the effect of crystal orientation on hotspot formation. Conclusions and directions for future work are discussed in Sec. IV.

II. GOVERNING EQUATIONS AND NUMERICAL METHODS

A. Global conservation laws and constitutive models

The conservation laws for mass, momentum, and energy to model the shock response of an anisotropic EM crystal are cast in the Eulerian form,[1,22,35] viz.,

$$\frac{\partial \rho}{\partial t} + (\rho u_i)_{,i} = 0, \tag{1}$$

$$\frac{\partial (\rho u_i)}{\partial t} + (\rho u_i u_j + p\delta_{ij})_{,j} = S_{ij,j}, \tag{2}$$

$$\frac{\partial (\rho E)}{\partial t} + (\rho E u_j + p u_j)_{,j} = (u_i S_{ij})_{,j}, \tag{3}$$

where ρ and u_i are the density and the velocity components; $E = e + \frac{1}{2} u_i u_i$ is the specific total energy and e is the specific internal energy. The temperature, T, is computed from e via the caloric equation of state

$$T = T_{ref} + \frac{e - e_{ref}}{C_v}, \tag{4}$$

where C_v is the specific heat and T_{ref} and e_{ref} are the reference temperature and the reference specific internal energy, respectively. In Eqs. (2) and (3), the Cauchy stress tensor, σ_{ij}, is decomposed additively as $\sigma_{ij} = -p\delta_{ij} + S_{ij}$, where p is an isotropic thermodynamic pressure expressed as a function of density and internal energy via an equation of state (EOS), and S_{ij} is a coupling stress related to the isochoric strain-rate tensor via a linear, anisotropic constitutive model.[19] The constitutive models are identical to that of the Lagrangian framework of Ref. 18, which, in turn, was calibrated against the MD calculations of Ref. 19.

The pressure is described by an EOS of the Mie–Grüniesen form

$$p(e, \rho) = \Gamma\rho(e - e_{ref}(\rho)) + p_{ref}(\rho) = \Gamma\rho e + f(\rho), \tag{5}$$

Γ is the Grüneisen parameter defined as $\Gamma\rho = \Gamma_0\rho_0$, where ρ_0 is the reference density of the unstressed material and Γ_0 is the reference value of the Grüneisen parameter. In Eq. (5), the reference internal energy e_{ref} and the reference pressure p_{ref} depend on the density only and are often combined into a single function, $f(\rho)$, which is fit to Hugoniot data,[19]

$$f(\rho) = \begin{cases} p_{ref}(\rho) - \Gamma\rho e_{ref}(\rho) = \dfrac{c_0^2\rho_0\phi}{(1 - s\phi)^2}\left[1 - \dfrac{\Gamma}{2}\left(\dfrac{\rho}{\rho_0} - 1\right)\right] & \text{for } \rho \geq \rho_0 \\ = c_0^2(\rho - \rho_0), & \text{for } \rho < \rho_0, \end{cases} \tag{6}$$

where $\phi = 1 - \frac{\rho_0}{\rho}$, s is the slope of the Hugoniot, c_0 is the bulk speed of sound, given by $c_0^2 = \frac{K_0}{\rho_0}$, and K_0 is the bulk modulus.

The coupling stress S_{ij} is evolved using a hypo-elastic description given by

$$\frac{\partial (\rho S_{ij})}{\partial t} + (\rho u_k S_{ij})_{,k} - \rho S_{ik} L_{kj} - \rho L_{ik} S_{kj} + \rho D_{kk} S_{ij} = \rho C_{ijkl} D^e_{kl} - \rho\left(\frac{1}{9} C_{kkll}\right) D_{pp}\delta_{ij}, \tag{7}$$

where C_{ijkl} are the elastic constants in the current coordinates with the invariant $\frac{1}{9} C_{kkll}$ being the bulk modulus K_0, $L_{ij} = u_{i,j}$ are the components of the velocity gradient tensor, and $D_{ij} = \frac{1}{2}(L_{ij} + L_{ji})$ is the strain-rate tensor. The left-hand side of Eq. (7) is the Truesdell rate of the coupling stress, S_{ij}, while the last term on the right-hand side of the equation removes the contribution of the volumetric strain-rate to the evolution of S_{ij} since the equation of state [Eq. (5)] already accounts for the stresses due to the volumetric strain. Note that unlike isotropic materials (or crystals with cubic symmetry), the coupling stress S_{ij} is not trace-free. In other words, a purely deviatoric deformation induces a volumetric stress, which is equal to $-S_{ii}/3$. Thus, the total volumetric stress of the material is the sum of the thermodynamic pressure and the trace of the coupling stress, which arise from purely volumetric and deviatoric deformations, respectively.

Note that Eq. (7) is a hypo-elastic model relating the evolution of S_{ij} to the isochoric strain-rates. While hyper-elastic models have also been used in Eulerian elastoplastic formulations,[9,36] they have been limited to isotropic constitutive descriptions of the elasticity in the material, i.e., where the Helmholtz free energy can be decomposed into dilatational and deviatoric components.[37] For an anisotropic material, such a decomposition of the free energy is non-trivial in an Eulerian frame of reference. Additionally, hypo-elastic descriptions present computational advantages, especially for reactive multi-material systems under shocks. For reactive

systems such as HEs or structural reactive materials,[38] thermodynamic closures (such as pressure-temperature equilibrium) are prescribed in terms of stress components in a partially reacted/mixed-cell. Since stresses are the primary variables in hypo-elastic formulations, incorporating thermodynamic closures is also relatively straightforward. The drawback is that with the exception of specific choices of the tangent modulus (see Kratochvil *et al.*[31]), hypo-elastic formulations are not inherently isentropic. However, for moderate to strong shocks and for other high strain-rate processes, the irreversible isochoric hypo-elastic stresses are small compared to the pressure. A comparison of hypo-elastic and hyper-elastic computations by Brepols *et al.*[39] showed that for a wide variety of loading conditions, hypo-elastic formulations yield stresses, which are in good agreement with hyper-elastic computations. Because of its compatibility with the Eulerian framework, this work adopts a hypo-elastic model [Eq. (7)] for describing the isochoric elasticity of the material and extension to include hyper-elastic constitutive models for reactive anisotropic multi-material systems is left to future work.

To close Eq. (7), the deviatoric strain-rate tensor, $D^d_{ij} \equiv D_{ij} - \frac{1}{3}D_{kk}\delta_{ij}$, is additively decomposed into elastic and plastic parts, D^e_{ij} and D^p_{ij}, in a Prandtl–Reuss model, respectively,[40,41]

$$D^d_{ij} = D^e_{kl} + D^p_{ij}. \tag{8}$$

The plastic strain rate D^p_{ij} is obtained from the sum of the shear strain rates, $\dot{\gamma}^\alpha$, along the individual slip systems as follows:

$$D^p_{ij} = \frac{1}{2}\sum_{\alpha=1}^{n} \dot{\gamma}^\alpha (s^\alpha_i n^\alpha_j + s^\alpha_j n^\alpha_i). \tag{9}$$

In Eq. (9), n is the total number of slip systems in the crystal, while n^α_i and s^α_i are the components of the unit normals and the glide direction unit vectors of the α^{th} slip-system in the current configuration. Note that Eq. (7) demands that the elastic constants C_{ijkl} be in the current coordinate system. Furthermore, in Eq. (9), n^α_i and s^α_i—which are also typically specified in the material coordinate system—are pushed forward to the current coordinates throughout the process of deformation. The procedure for updating the elastic constants, glide directions, and unit normals in the current coordinates is described next.

B. Initialization and update of the elastic constants, glide directions, and unit normals

Figure 1 shows an example of a monoclinic crystal such as β-HMX, with the unit-cell vectors $\boldsymbol{a}$, $\boldsymbol{b}$, and $\boldsymbol{c}$ in the fractional coordinates. The dimensions of the crystal lattices are l_1, l_2, and l_3, and the vectors $\boldsymbol{a}$ and $\boldsymbol{c}$ are at angle of $\beta(\neq 90^\circ)$ ($\boldsymbol{a}$, $\boldsymbol{c}$ are not orthogonal to each other), as shown in the figure. We define a Cartesian coordinate system locally within the unit cell, with unit vectors $\boldsymbol{e}'_1$, $\boldsymbol{e}'_2$, and $\boldsymbol{e}'_3$, such that $\boldsymbol{e}'_1$ and $\boldsymbol{e}'_2$ are parallel to $\boldsymbol{a}$ and $\boldsymbol{b}$, respectively. The elastic constants are typically specified in the Cartesian coordinate system spanned by $\boldsymbol{e}'_1$, $\boldsymbol{e}'_2$, and $\boldsymbol{e}'_3$ and are denoted by $\tilde{C}_{ijkl}$, where the tilde is used to distinguish the elastic constants in the unit cell basis ($\boldsymbol{e}'_1$, $\boldsymbol{e}'_2$, $\boldsymbol{e}'_3$) from those in the global Cartesian coordinate system. Furthermore, the glide directions and the unit normals of the slip and loading planes are specified in Miller indices, i.e., in the non-orthogonal, fractional coordinate system spanned by $\boldsymbol{a}$, $\boldsymbol{b}$, and $\boldsymbol{c}$. The procedure for mapping the glide directions and the unit normals under the assumption of small elastic stretches onto a Cartesian system is briefly described next.

Figure 1 shows a representative slip plane of the crystal with a glide direction $\bar{\boldsymbol{s}}^\alpha$ and a unit normal $\bar{\boldsymbol{n}}^\alpha \equiv (h^\alpha k^\alpha l^\alpha)$, with respect to the fractional coordinate system. $\bar{\boldsymbol{s}}^\alpha$ and $\bar{\boldsymbol{n}}^\alpha$ are mapped from the fractional coordinate system into the ($\boldsymbol{e}'_1$, $\boldsymbol{e}'_2$, $\boldsymbol{e}'_3$) Cartesian coordinate system via a transformation matrix, $\mathbf{R}^{(1)}$, defined as

$$\mathbf{R}^{(1)} = \begin{bmatrix} l_1 & 0 & l_3\cos\beta \\ 0 & l_2 & 0 \\ 0 & 0 & l_3\sin\beta \end{bmatrix}. \tag{10}$$

The glide direction, $\bar{\boldsymbol{s}}^\alpha$, defined in the fractional coordinate system is mapped onto the glide direction $\tilde{\mathbf{s}}^\alpha$ in the ($\boldsymbol{e}'_1$, $\boldsymbol{e}'_2$, $\boldsymbol{e}'_3$) coordinate system using the transformation, $\tilde{\mathbf{s}}^\alpha = \mathbf{R}^{(1)}\bar{\boldsymbol{s}}^\alpha$. Similarly, the unit-cell vectors, $\boldsymbol{a}$, $\boldsymbol{b}$, and $\boldsymbol{c}$ are transformed into the ($\boldsymbol{e}'_1$, $\boldsymbol{e}'_2$, $\boldsymbol{e}'_3$) coordinate system via the same transformation $\tilde{\boldsymbol{a}} = \mathbf{R}^{(1)}\boldsymbol{e}'_1$, $\tilde{\boldsymbol{b}} = \mathbf{R}^{(1)}\boldsymbol{e}'_2$, and $\tilde{\boldsymbol{c}} = \mathbf{R}^{(1)}\boldsymbol{e}'_3$. The reciprocals of $\tilde{\boldsymbol{a}}$, $\tilde{\boldsymbol{b}}$, and $\tilde{\boldsymbol{c}}$, denoted by $\tilde{\boldsymbol{a}}^*$, $\tilde{\boldsymbol{b}}^*$, and $\tilde{\boldsymbol{c}}^*$ are computed using[31]

$$\tilde{\boldsymbol{a}}^* = \frac{\tilde{\boldsymbol{b}}\times\tilde{\boldsymbol{c}}}{\tilde{\boldsymbol{a}}.(\tilde{\boldsymbol{b}}\times\tilde{\boldsymbol{c}})}, \quad \tilde{\boldsymbol{b}}^* = \frac{\tilde{\boldsymbol{c}}\times\tilde{\boldsymbol{a}}}{\tilde{\boldsymbol{b}}.(\tilde{\boldsymbol{c}}\times\tilde{\boldsymbol{a}})}, \quad \tilde{\boldsymbol{c}}^* = \frac{\tilde{\boldsymbol{a}}\times\tilde{\boldsymbol{b}}}{\tilde{\boldsymbol{c}}.(\tilde{\boldsymbol{a}}\times\tilde{\boldsymbol{b}})}. \tag{11}$$

These vectors are, in turn, used to map $\bar{\boldsymbol{n}}^\alpha$ onto the unit-normal direction $\tilde{\mathbf{n}}^\alpha$ in the ($\boldsymbol{e}'_1$, $\boldsymbol{e}'_2$, $\boldsymbol{e}'_3$) coordinate system as follows:

$$\tilde{\mathbf{n}}^\alpha = h^\alpha\tilde{\boldsymbol{a}}^* + k^\alpha\tilde{\boldsymbol{b}}^* + l^\alpha\tilde{\boldsymbol{c}}^*. \tag{12}$$

The same procedure is also followed to map the unit normal of the loading plane from the fractional (a, b, c) to the ($\boldsymbol{e}'_1$, $\boldsymbol{e}'_2$, $\boldsymbol{e}'_3$) coordinate system; the loading unit normal direction in the ($\boldsymbol{e}_1$, $\boldsymbol{e}_2$, $\boldsymbol{e}_3$) system is denoted by $\tilde{\mathbf{n}}^0$. Thus, after these mappings, similar to $\tilde{C}_{ijkl}$, $\tilde{\mathbf{s}}^\alpha$ and $\tilde{\mathbf{n}}^\alpha$ are also defined in the Cartesian coordinate system spanned by the unit-cell Cartesian basis ($\boldsymbol{e}'_1$, $\boldsymbol{e}'_2$, $\boldsymbol{e}'_3$).

Although $\tilde{C}_{ijkl}$, $\tilde{\mathbf{s}}^\alpha$, and $\tilde{\mathbf{n}}^\alpha$ are all described in the ($\boldsymbol{e}'_1$, $\boldsymbol{e}'_2$, $\boldsymbol{e}'_3$) Cartesian coordinate system, for arbitrary loading directions, the ($\boldsymbol{e}'_1$, $\boldsymbol{e}'_2$, $\boldsymbol{e}'_3$) Cartesian coordinate system does not necessarily coincide with the global Cartesian coordinate system spanned by ($\boldsymbol{e}_1$, $\boldsymbol{e}_2$, $\boldsymbol{e}_3$) in which the global conservation laws [Eqs. (1) through (3)] are cast. Therefore, $\tilde{C}_{ijkl}$, $\tilde{\mathbf{s}}^\alpha$ and $\tilde{\mathbf{n}}^\alpha$ need to be mapped from the ($\boldsymbol{e}'_1$, $\boldsymbol{e}'_2$, $\boldsymbol{e}'_3$) coordinate system to that spanned by ($\boldsymbol{e}_1$, $\boldsymbol{e}_2$, $\boldsymbol{e}_3$). To perform this mapping, a second transformation matrix, $\mathbf{R}^{(2)}$, is defined such that the unit normal of the loading plane $\tilde{\mathbf{n}}^0$ [defined in the ($\boldsymbol{e}'_1$, $\boldsymbol{e}'_2$, $\boldsymbol{e}'_3$) coordinate system] aligns with $\tilde{\mathbf{n}}$, which is the desired loading direction in the ($\boldsymbol{e}_1$, $\boldsymbol{e}_2$, $\boldsymbol{e}_3$) coordinate system. This matrix, $\mathbf{R}^{(2)}$, is obtained using Rodrigues' rotation formula

$$\mathbf{R}^{(2)} = \mathbf{I} + \mathbf{A} + \frac{1-c}{s^2}\mathbf{A}^2; \quad \mathbf{A} = \begin{bmatrix} 0 & -a_3 & a_2 \\ a_3 & 0 & -a_1 \\ -a_2 & a_1 & 0 \end{bmatrix}, \tag{13}$$

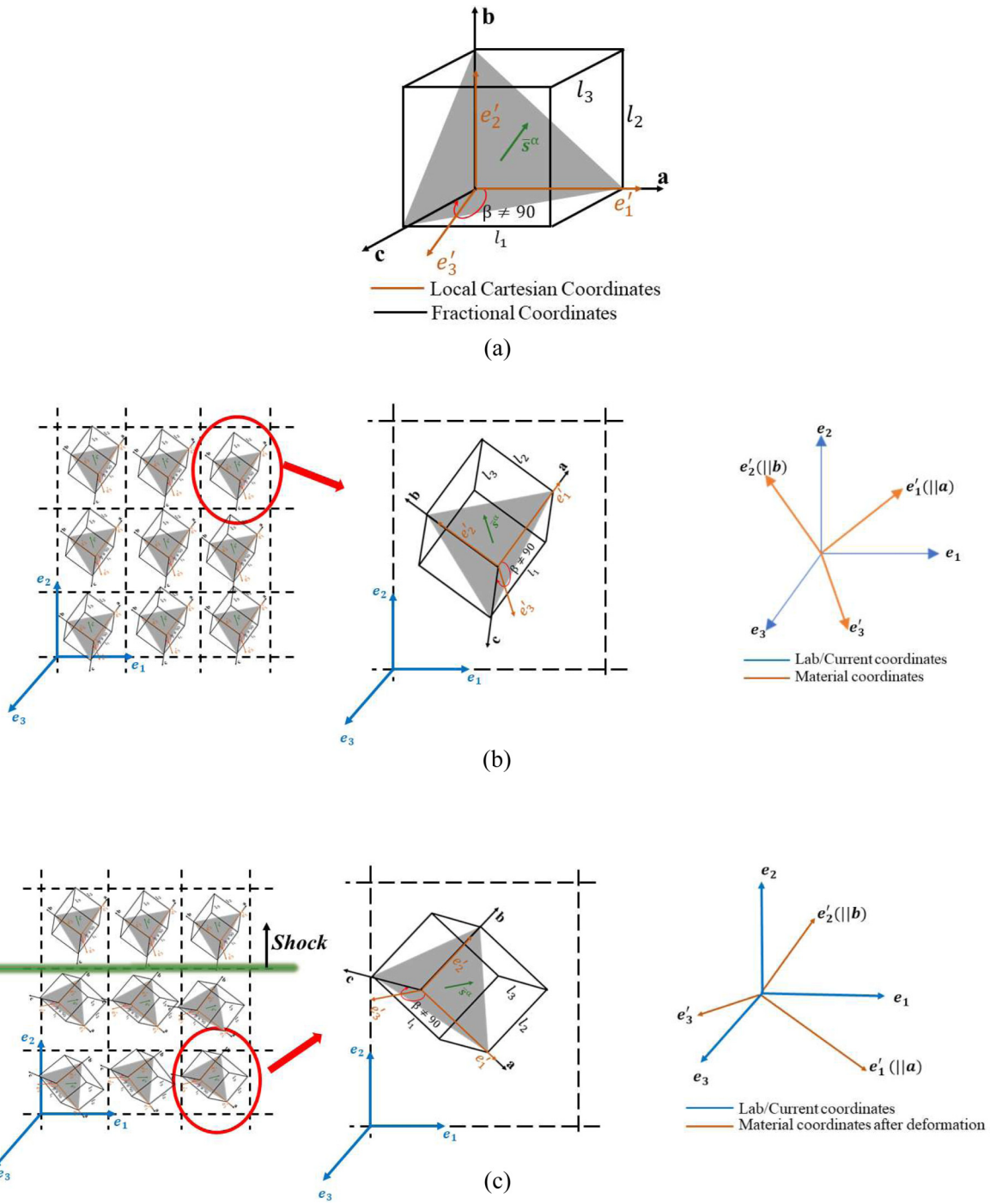

FIG. 1. (a) Schematic representation of a single-crystal of β-HMX. l_1, l_2, and l_3 are the lengths of the crystal lattice, and **a**, **b**, and **c** are the basis-vectors in the fractional coordinate system defined such that they are parallel to the three-lattice directions. $\boldsymbol{e}'_1$, $\boldsymbol{e}'_2$, and $\boldsymbol{e}'_3$ define a local Cartesian coordinate system such that $\boldsymbol{e}'_1$ and $\boldsymbol{e}'_2$ are parallel to **a** and **b**, respectively. The shaded plane is an example of a candidate slip-system of the crystal, with $\bar{\boldsymbol{s}}^{\boldsymbol{\alpha}}$ being the glide direction. (b) and (c) Schematic representation of the orientation of the crystal lattice with respect to the Cartesian grid for solving the global conservation laws. The global Cartesian system is spanned by $\boldsymbol{e}_1$, $\boldsymbol{e}_2$, and $\boldsymbol{e}_3$. (b) shows the orientation at $\boldsymbol{t} = 0$, while (c) shows the orientation at an arbitrary time during shock passage. Both these schematics are zoomed in to show the relative orientations of the crystal with respect to the grid.

where $\mathbf{I}$ is the 3×3 identity matrix, $c = \tilde{\mathbf{n}}^0.\tilde{\mathbf{n}}$, $\mathbf{a} = \tilde{\mathbf{n}} \times \tilde{\mathbf{n}}^0 = \lfloor a_1 \quad a_2 \quad a_3 \rfloor$, $s = |\mathbf{a}|$. Once $\mathbf{R}^{(2)}$ is computed for specified values of $\tilde{\mathbf{n}}^0$ and $\tilde{\mathbf{n}}$, the glide directions, $\mathbf{s}^\alpha$, and the directions of the unit normals, $\mathbf{n}^\alpha$, in the $(\boldsymbol{e}_1, \boldsymbol{e}_2, \boldsymbol{e}_3)$ co-ordinate systems are given by $\mathbf{s}^\alpha = \mathbf{R}^{(2)}\tilde{\mathbf{s}}^\alpha$ and $\mathbf{n}^\alpha = \mathbf{R}^{(2)}\tilde{\mathbf{n}}^\alpha$. To map the elastic constants, $\tilde{C}_{ijkl}$, from the $(\boldsymbol{e}_1', \boldsymbol{e}_2', \boldsymbol{e}_3')$ coordinate system to the $(\boldsymbol{e}_1, \boldsymbol{e}_2, \boldsymbol{e}_3)$ coordinate system, the direction cosines of the unit vectors $\boldsymbol{e}_1$, $\boldsymbol{e}_2$, and $\boldsymbol{e}_3$ are computed with respect to the crystal-fixed coordinate system, $(\boldsymbol{e}_1', \boldsymbol{e}_2', \boldsymbol{e}_3')$. The direction cosines of $\boldsymbol{e}_1$, denoted by (k_1, k_2, k_3) are the components of the vector $\tilde{\boldsymbol{e}}_1 = \mathbf{R}^{(2)} \cdot \boldsymbol{e}_1'$, i.e., the components of $\tilde{\boldsymbol{e}}_1$ are the projections of $\boldsymbol{e}_1'$ in the $\boldsymbol{e}_1$, $\boldsymbol{e}_2$, and $\boldsymbol{e}_3$ directions. Similarly, (m_1, m_2, m_3) and (n_1, n_2, n_3), which are the direction cosines of $\boldsymbol{e}_2$ and $\boldsymbol{e}_3$ are the components of the vectors $\tilde{\boldsymbol{e}}_2 = \mathbf{R}^{(2)} \cdot \boldsymbol{e}_2'$ and $\tilde{\boldsymbol{e}}_3 = \mathbf{R}^{(2)} \cdot \boldsymbol{e}_3'$, respectively; similarly, $\tilde{\boldsymbol{e}}_2$ and $\tilde{\boldsymbol{e}}_3$ are also the respective projections of $\boldsymbol{e}_2'$ and $\boldsymbol{e}_3'$ in the $\boldsymbol{e}_1$, $\boldsymbol{e}_2$, and $\boldsymbol{e}_3$ directions [see Fig. 1(b) for an illustration]. These direction cosines are used to define a 6×6 matrix[42]

$$\mathbf{Q} = \begin{bmatrix} k_1^2 & k_2^2 & k_3^2 & 2k_2k_3 & 2k_3k_1 & 2k_1k_2 \\ m_1^2 & m_2^2 & m_3^2 & 2m_2m_3 & 2m_3m_1 & 2m_1m_2 \\ n_1^2 & n_2^2 & n_3^2 & 2n_2n_3 & 2n_3n_1 & 2n_1n_3 \\ m_1n_1 & m_2n_2 & m_3n_3 & m_2n_3 + n_2m_3 & m_3n_1 + n_3m_1 & m_2n_1 + n_2m_1 \\ n_1k_1 & n_2k_2 & n_3k_3 & n_2k_3 + k_2n_3 & n_3k_1 + k_3n_1 & n_2k_1 + k_2n_1 \\ k_1m_1 & k_2m_2 & k_3m_3 & k_2m_3 + m_2k_3 & k_3m_1 + m_3k_1 & m_1k_2 + k_1m_2 \end{bmatrix}. \tag{14}$$

The above matrix $\mathbf{Q}$ is used to compute C_{ijkl} from $\tilde{C}_{ijkl}$ via the transformation $\mathbb{C} = \mathbf{Q}\tilde{\mathbb{C}}\mathbf{Q}^T$, where $\mathbb{C}$ and $\tilde{\mathbb{C}}$ are comprised of the elastic constants C_{ijkl} and $\tilde{C}_{ijkl}$, expressed in the Voigt notation. Following the above operations, the elastic constants are also expressed in the current $(\boldsymbol{e}_1, \boldsymbol{e}_2, \boldsymbol{e}_3)$ coordinate system.

As the shock-induced deformation of the crystal proceeds, it is necessary to track C_{ijkl}, $\mathbf{s}^\alpha$, and $\mathbf{n}^\alpha$ throughout the process of deformation (as shown in Fig. 2). To this end, the unit vectors $\tilde{\boldsymbol{e}}_1$ and $\tilde{\boldsymbol{e}}_2$ are evolved via the following equations:

$$\frac{\partial(\rho\tilde{e}_1 i)}{\partial t} + (\rho u_j \tilde{e}_1 i)_{,j} = \rho L_{ij}^e \tilde{e}_1 j, \tag{15a}$$

$$\frac{\partial(\rho\tilde{e}_2 i)}{\partial t} + (\rho u_j \tilde{e}_2 i)_{,j} = -\rho L_{ji}^e \tilde{e}_2 j. \tag{15b}$$

Equation (15) represent the rate-form of the push-forward operations, $\tilde{\boldsymbol{e}}_1 = \mathbf{F}^e\tilde{\boldsymbol{e}}_1^0$ and $\tilde{\boldsymbol{e}}_2 = \mathbf{F}^{e-T}\tilde{\boldsymbol{e}}_2^0$, written in conservation form.[43] Here, $\mathbf{F}^e$ is the elastic component of the deformation gradient, while $\tilde{\boldsymbol{e}}_1^0$ and $\tilde{\boldsymbol{e}}_2^0$ are the projections of the Cartesian unit cell basis vectors in the reference coordinate system. Once $\tilde{\boldsymbol{e}}_1$ and $\tilde{\boldsymbol{e}}_2$ are computed using Eq. (15), $\tilde{\boldsymbol{e}}_3$ is obtained as the vector cross-product: $\tilde{\boldsymbol{e}}_3 = \tilde{\boldsymbol{e}}_1 \times \tilde{\boldsymbol{e}}_2$. After computing $\tilde{\boldsymbol{e}}_1$, $\tilde{\boldsymbol{e}}_2$, and $\tilde{\boldsymbol{e}}_3$, the updated direction cosines (k_1, k_2, k_3), (m_1, m_2, m_3), and (n_1, n_2, n_3) are used to re-define the matrix $\mathbf{Q}$ using Eq. (14), which, in turn, is used to transform $\tilde{C}_{ijkl}$ into the current coordinate system after deformation. These updated elastic constants, C_{ijkl}, are then used in Eq. (7) to compute the coupling stresses, S_{ij}.

Similar to $\tilde{\boldsymbol{e}}_1$ and $\tilde{\boldsymbol{e}}_2$, the rate-forms of the push-forward operations, $\mathbf{s}^\alpha = \mathbf{F}^e\mathbf{s}^{\alpha 0}$ and $\mathbf{n}^\alpha = \mathbf{F}^{e-T}\mathbf{n}^{\alpha 0}$ are used to evolve the glide directions and the directions of the unit normal during the process of deformation, where $\mathbf{s}^{\alpha 0}$ and $\mathbf{n}^{\alpha 0}$ are the glide directions and the unit normals in the reference coordinate system. The evolution equations of $\mathbf{s}^\alpha$ and $\mathbf{n}^\alpha$ are given by

$$\frac{\partial(\rho s_i^\alpha)}{\partial t} + (\rho u_j s_i^\alpha)_{,j} = \rho L_{ij}^e s_j^\alpha, \tag{16a}$$

$$\frac{\partial(\rho n_i^\alpha)}{\partial t} + (\rho u_j n_i^\alpha)_{,j} = -\rho L_{ji}^e n_j^\alpha, \tag{16b}$$

where $L_{ij}^e \equiv L_{ij} - L_{ij}^p$ is the elastic part of the velocity gradient tensor, and $L_{ij}^p = \sum_{\alpha=1}^{n} \dot{\gamma}^\alpha s_i^\alpha n_j^\alpha$ is the plastic part of the velocity gradient tensor. These updated glides and normals, computed using Eq. (16), are used to calculate the plastic strain-rate tensor in Eq. (9).

Remarks:

(i) The evolution equations described by Eqs. (15) and (16) are the rate-forms of the push-forward operations involving $\mathbf{s}^\alpha$, $\mathbf{n}^\alpha$, $\tilde{\boldsymbol{e}}_1$, and $\tilde{\boldsymbol{e}}_2$; these comprise a system of $6(n+1)$ partial differential equations, where each component of $\mathbf{s}^\alpha$, $\mathbf{n}^\alpha$, $\tilde{\boldsymbol{e}}_1$, and $\tilde{\boldsymbol{e}}_2$ is advected as a scalar variable with a source term on the right-hand side. These transport equations require boundary conditions, both at the domain boundaries as well as at multi-material interfaces. Determining the appropriate boundary conditions for these sub-grid scale crystallographic variables is non-trivial; to prevent spurious oscillations of $\tilde{\boldsymbol{e}}_1$, $\tilde{\boldsymbol{e}}_2$, $\mathbf{s}^\alpha$, and $\boldsymbol{n}^\alpha$, we assume the following Neumann boundary conditions for these variables:

$$\frac{\partial \mathbf{s}^\alpha}{\partial \boldsymbol{n}} = 0, \quad \frac{\partial \boldsymbol{n}^\alpha}{\partial \boldsymbol{n}} = 0, \quad \frac{\partial \tilde{\boldsymbol{e}}_1}{\partial \boldsymbol{n}} = 0, \quad \frac{\partial \tilde{\boldsymbol{e}}_2}{\partial \boldsymbol{n}} = 0, \tag{17}$$

where $\boldsymbol{n}$ is the unit normal at the domain/interfacial boundaries.

(ii) The conservation form of Eq. (16) is obtained by adding the continuity equation to the following rate equations: $\dot{\boldsymbol{s}}^{\boldsymbol{\alpha}} = \mathbf{L}^e\mathbf{s}^\alpha$ and $\dot{\mathbf{n}}^{\boldsymbol{\alpha}} = -\mathbf{L}^{\mathbf{e}\mathbf{T}}\mathbf{n}^\alpha$, where the dot denotes the

material derivative. These rate equations are total derivates of the push-forward operations: $\mathbf{s}^\alpha = \mathbf{F}^e\mathbf{s}^{\alpha 0}$ and $\mathbf{n}^\alpha = \mathbf{F}^{e-T}\mathbf{n}^{\alpha 0}$. $\mathbf{s}^\alpha$ and $\mathbf{n}^\alpha$ remain orthogonal after their transport via Eq. (16). This is because

$$(s_i\dot{n}_i) = \dot{s}_i n_i + s_i\dot{n}_i = L^e_{ij}s_j n_i - s_i L^e_{ji}n_j = L^e_{ij}s_j n_i - L^e_{ij}s_j n_i = 0. \tag{18}$$

Thus, Eq. (18) shows that the angle between $\mathbf{s}^\alpha$ and $\mathbf{n}^\alpha$ does not change after the evolution of the glides and unit normal directions via Eq. (16). However, in practice, advection errors accumulate with time due to the spatial discretization of the terms $(\rho u_j s_i^\alpha)_{,j}$ and $(\rho u_j n_i^\alpha)_{,j}$. This can result in non-orthogonality of the glide-directions and the unit normals, and the plastic strain-rate may develop a non-zero trace; i.e., D^p_{ii} in Eq. (9) may no longer be zero and the plastic strain-rate no longer isochoric. To ensure that the plastic-strain is isochoric (i.e., D^p_{ij} remains trace-free after evolving $\mathbf{s}^\alpha$ and $\mathbf{n}^\alpha$), $\mathbf{s}^\alpha$ and $\mathbf{n}^\alpha$ are corrected via the Gram–Schmidt orthonormalization after solving Eq. (16). In other words, $\mathbf{s}^\alpha$ and $\mathbf{n}^\alpha$ are first evolved using Eq. (16) and then $\mathbf{s}^\alpha$ is normalized to ensure $|\mathbf{s}^\alpha| = 1$. Finally, the advected $\mathbf{n}^\alpha$ is corrected via the Gram–Schmidt orthogonalization to ensure that $|\mathbf{n}^\alpha| = 1$ as well as $\mathbf{s}^\alpha \cdot \mathbf{n}^\alpha = 0$ after the transport via Eq. (16). Note that previous works on Eulerian crystal plasticity[30,31] did not employ a post-advection normalization of $\mathbf{s}^\alpha$ and $\mathbf{n}^\alpha$ as presumably the advection errors were small in the types of deformations considered in those works. The same normalization procedure is also followed for $\tilde{\boldsymbol{e}}_1$ and $\tilde{\boldsymbol{e}}_2$ to ensure that the crystallographic axes remain orthonormal throughout the process of deformation.

(iii) Finally, we note that unlike previous works on Eulerian crystal plasticity,[30,31] the current formulation takes into account the transformation of the elastic constants in the post-shock region, which is done by updating the lattice basis vectors, $\tilde{\boldsymbol{e}}_1$, $\tilde{\boldsymbol{e}}_2$, and $\tilde{\boldsymbol{e}}_3$ during the deformation.

TABLE I. The glide directions, the directions of the unit normals, and the strength-ratios for the slip-systems of β-HMX. The glide directions and the directions of the unit normals are in Miller notations in the $P2_1/n$ space group.

Slip system index, α	$\bar{\boldsymbol{s}}^\alpha$	$\bar{\boldsymbol{n}}^\alpha$	r^α
1	$[\bar{1}00]$	$(0\bar{1}0)$	1
2	$[100]$	$(0\bar{1}\bar{1})$	0.963
3	$[\bar{1}00]$	$(0\bar{1}1)$	0.963
4	$[0\bar{1}0]$	(101)	0.933
5	$[\bar{1}00]$	(001)	1.681
6	$[\bar{1}01]$	(101)	0.376
7	$[\bar{1}1\bar{1}]$	(011)	0.931
8	$[111]$	$(0\bar{1}1)$	0.931
9	$[001]$	$(\bar{1}10)$	0.701
10	$[00\bar{1}]$	(110)	0.701

C. Flow rule for the shear strain rates

Following the works of Duarte *et al.*[19] the plastic strain-rate, $\dot{\gamma}^\alpha$, is modeled using a power-law form[44,45]

$$\dot{\gamma}^\alpha = \min\left\{\dot{\gamma}^0 \mathrm{sign}(\tau_s^\alpha)\left|\frac{\tau_s^\alpha}{\tau_{th}^\alpha}\right|^{1/m}, \quad \dot{\gamma}_0^{pd}\right\}, \tag{19}$$

where $\dot{\gamma}^0$ is the reference slip-rate, $\tau_s^\alpha = S_{ij}s_i^\alpha n_j^\alpha$ is the resolved shear stress on the αth slip-system, m is the rate-sensitivity parameter, and τ_{th}^α is the threshold slip resistance of the αth slip-system. It is assumed that $\dot{\gamma}^\alpha$ is limited by the phonon-drag limit, $\dot{\gamma}_0^{pd}$, which is taken to be $2.5\,\mathrm{ns}^{-1}$ following Duarte *et al.*[19] The threshold slip resistance, τ_{th}^α, follows the hardening rule

$$\tau_{th}^\alpha = r^\alpha g_s^\alpha, \tag{20}$$

where r^α is the strength ratio on each slip-system and g_s^α is the resistance to slip, which evolves according to

$$\dot{g}_s^\alpha = \sum_{\beta=1}^{n} h_{\alpha\beta}\left|1 - \frac{g_s^\beta}{g_{sat}}\right|^a \mathrm{sign}\left(1 - \frac{g_s^\beta}{g_{sat}}\right)\dot{\gamma}^\beta. \tag{21}$$

In the above, a is the hardening exponent, g_{sat} is the saturation slip resistance, and $h_{\alpha\beta}$ is the hardening matrix, taken to be $h_0\delta_{\alpha\beta}$ as in Duarte *et al.*[19] Note that since $\dot{g}_s^\alpha = \frac{\partial g_s^\alpha}{\partial t} + u_i\frac{\partial g_s^\alpha}{\partial x_i}$, Eq. (21) comprises a set of additional n partial differential equations; similar to $\mathbf{s}^\alpha$, $\mathbf{n}^\alpha$, $\tilde{\boldsymbol{e}}_1$, and $\tilde{\boldsymbol{e}}_2$, zero-gradient boundary conditions of the form

$$\frac{\partial g_s^\alpha}{\partial \boldsymbol{n}} = 0 \tag{22}$$

are assumed for the slip resistance at all domain boundaries and interfaces.

D. Comparison of Eulerian and Lagrangian approaches

In Sec. III, the present Eulerian calculations are compared to the Lagrangian finite element approach to simulate the shock response of β-HMX. It is noted that while there are several material models available for single crystal plasticity of HE crystals under shocks,[3,6,10] we chose the model described above as it allowed for benchmarking the Eulerian computational framework against calculations performed with a traditional Lagrangian crystal plasticity framework. The above model, originally developed in Ref. 5, was shown to capture the anisotropic response of HMX accurately and has been validated against experiments[18] as well as MD calculations.[19] The above glide-based material model will be used to directly compare the individual anisotropic stress components in shocked β-HMX calculated from the previously validated Lagrangian approach with the values calculated from the current Eulerian framework. Investigation of other types of crystal plasticity models[10,17] and their Eulerian implementations is currently being performed and will be reported in future work. The material model employed by the Lagrangian calculations was calibrated against molecular dynamics (MD) simulations in previous publications.[5,18,19] The Lagrangian calculations are performed using the

TABLE II. Values of the material properties of β-HMX. The values of the lattice parameters are in the $P2_1/n$ space group.

Reference density, ρ_0 (kg m^{-3})	Isochoric specific heat, C_v (J kg^{-1} K^{-1})	Reference Grüneisen coefficient, Γ_0	Slope of the Hugoniot, s	Bulk modulus, K_0 (GPa)	Lattice length, l_1 (Å)	Lattice lengthl_2 (Å)
1850	2357.3	0.7	2.29	14.24	6.54	11.03
Lattice length, l_3(Å)	Lattice angle, β(deg)	$\tilde{\mathbb{C}}_{11}$(GPa)	$\tilde{\mathbb{C}}_{22}$(GPa)	$\tilde{\mathbb{C}}_{33}$(GPa)	$\tilde{\mathbb{C}}_{44}$(GPa)	$\tilde{\mathbb{C}}_{55}$(GPa)
7.35	102.8	20.78	20.54	21.10	8.7	5.57
$\tilde{\mathbb{C}}_{66}$(GPa)	$\tilde{\mathbb{C}}_{12}$(GPa)	$\tilde{\mathbb{C}}_{13}$(GPa)	$\tilde{\mathbb{C}}_{23}$(GPa)	$\tilde{\mathbb{C}}_{15}$(GPa)	$\tilde{\mathbb{C}}_{25}$(GPa)	$\tilde{\mathbb{C}}_{35}$(GPa)
10.62	10.05	9.36	13.46	4.46	6.81	5.56
$\tilde{\mathbb{C}}_{46}$(GPa)	Reference shear strain rate, $\dot{\gamma}_0$(ns^{-1})	Stress exponent, m	Phonon drag limit, $\dot{\gamma}_0^{pd}$ (ns^{-1})	Hardening constant, h_0(MPa)	Hardening exponent, a	Saturation slip resistance, g_{sat}(MPa)
4.39	0.001	0.1	2.5	2.34	2.5	155.73
Initial glide stress, g_s^0(MPa)	Reference temperature, T_{ref}(K)	Reference internal energy, e_{ref} (J/kg)	Artificial viscosity constant, C_0	Artificial viscosity constant, C_1	Artificial viscosity constant, C_2	Artificial viscosity constant, C_3
103.03	298	0	0.1	1.0	0.0055	0.055

multi-physics finite element software MOOSE[46] using the MD-derived material models. The anisotropic crystal plasticity model parameters are listed in Tables I and II, and identical models are employed in both the Eulerian and Lagrangian calculations.

The Lagrangian formulation and computational algorithm has been described in detail in previously published work[5,18,19] and is not reproduced here. Instead, we summarize below the following key differences between the Lagrangian and the current Eulerian frameworks that are relevant to the current work:

1. The Lagrangian model employs a hyperelastic formulation, where the deformation gradient, $\mathbf{F}$ is decomposed multiplicatively as $\mathbf{F} = \mathbf{F^e F^p}$, where $\mathbf{F^e}$ is the elastic component of the deformation gradient and $\mathbf{F^p}$ is the plastic component obtained by integrating the plastic strain-rate tensor defined in Eq. (9). In contrast, the Eulerian framework is based on a hypo-elastic formulation, which obviates the computation of $\mathbf{F}$ and directly relies on an additive decomposition of the strain-rate tensor as shown in Eq. (8).
2. In Lagrangian computations, the second Piola–Kirchoff stress, $\mathbf{P}$, is computed directly from a hyper-elastic constitutive model; these are then pushed forward to the current coordinate system to compute the Cauchy stresses. In the current Eulerian framework, the Cauchy stresses are computed from Eq. (7), while the elastic constants are mapped into the current coordinate system in the hypo-elastic constitutive model.
3. The Lagrangian computations employ a finite element method for spatial discretization, which can experience oscillations at shocks and other discontinuities. Artificial viscous stresses are used to obtain smooth solutions; consequently, the second Piola–Kirchoff stress tensor, $\mathbf{P}$ consists of three stress components, viz., $\mathbf{P} = \mathbf{P^{coupling}} + \mathbf{P^{eos}} + \mathbf{P^{viscous}}$. The first stress component, $\mathbf{P^{coupling}}$, is the stress which accounts for isochoric stretches due to material anisotropy and is the pull-back of coupling stress, $\mathbf{S}$, described in Sec. II A. The second component, $\mathbf{P^{eos}}$, is the pull-back of $p\delta_{ij}$, where the pressure, p, is defined by Eq. (5). The third component, $\mathbf{P^{viscous}}$, is the artificial viscous stress tensor modeled as follows:

$$\mathbf{P^{viscous}} = C_0\rho_0 \frac{\dot{J}|\dot{J}|}{J^2} h^2\mathbf{I} + C_1\rho_0 c_0 \frac{\dot{J}}{J} h\mathbf{I}, \tag{23}$$

where h is the element size, J is the Jacobian of the deformation gradient, $\mathbf{I}$ is the 3×3 identity matrix, and C_0 and C_1 are artificial viscosity coefficients used to distribute the shock front across a few elements. In contrast to the Lagrangian formulation, the current Eulerian framework uses a shock-capturing scheme (third-order ENO[47]) for spatial discretization. Since the ENO scheme implicitly satisfies the entropy condition, spurious oscillations do not arise at shocks and other discontinuities. Due to the use of shock-capturing schemes in the present Eulerian approach, artificial viscous stresses need not be introduced in the Eulerian calculations.[48,49] The implications of the differences in the numerical treatment of shocks are examined in the Results section.
4. Finally, the Lagrangian computational setup does not use embedded levelsets to represent the block of β-HMX but uses a

body-fitted finite element mesh to simulate the shock response. Furthermore, in the Lagrangian computation, a uniform velocity is directly prescribed at the south face of the material-block to initiate the shock in the material. A reverse ballistic impact is employed in the Eulerian calculations to mimic the boundary conditions imposed in the Lagrangian simulations. These differences in supplying boundary conditions are typical of Lagrangian and Eulerian formulations but have no observable impacts on the benchmarking exercise to study shock propagation through the material.

E. Numerical procedure for solving the governing equations

The overall system of equations for modeling single crystal plasticity of a material with n slip systems comprises a set of $17 + 7n$ partial differential equations, viz., 5 equations for the global conservation of mass, momentum and specific total internal energy [Eqs. (1)–(3)], 6 equations for the coupling-stress evolution [Eq. (7)], 6 equations for evolving each component of $\tilde{\boldsymbol{e}}_1$ and $\tilde{\boldsymbol{e}}_2$ [Eq. (15)], $6n$ equations for evolving each component of $\mathbf{s}^\alpha$ and $\mathbf{n}^\alpha$ [Eq. (16)], and n equations for evolving g_s^α [Eq. (21)]. These equations are closed by the equations of state [Eqs. (5) and (6)], the shear strain rate model [Eqs. (19) and (20)] and the definition of plastic strain rate [Eq. (9)], while the temperature is obtained as a passive scalar, via Eq. (4).

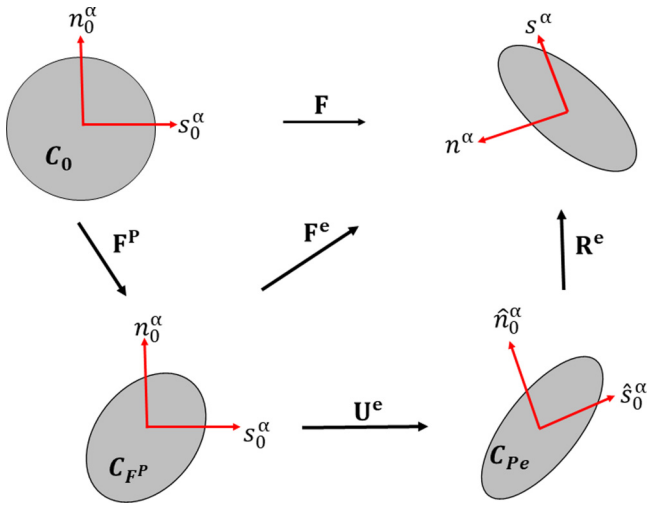

FIG. 2. Schematic conceptualization of the deformation of a material using crystal plasticity models. The original configuration is denoted by $\boldsymbol{C_0}$, the configuration after lattice shearing is denoted by $\boldsymbol{C_{F^P}}$, and the configuration after elastic stretching is denoted by $\boldsymbol{C_{P^e}}$. The deformation gradient, $\boldsymbol{F}$, is decomposed multiplcatively into elastic and plastic components, $\boldsymbol{F^e}$ and $\boldsymbol{F^P}$, via, $\boldsymbol{F = F^eF^P = R^eU^eF^P}$, where $\boldsymbol{R^e}$ and $\boldsymbol{U^e}$ are the elastic rotations and stretches. The original glide directions and directions for the unit normals are denoted by $\boldsymbol{s_o^\alpha}$ and $\boldsymbol{n_o^\alpha}$. It is assumed that lattice stretches do not alter $\boldsymbol{s_o^\alpha}$ and $\boldsymbol{n_o^\alpha}$; the elastic stretch changes the directions of glide and unit normals to $\hat{\boldsymbol{s}}_{\boldsymbol{o}}^{\boldsymbol{\alpha}}$ and $\hat{\boldsymbol{n}}_{\boldsymbol{o}}^{\boldsymbol{\alpha}}$, which are further rotated elastically to the final directions, $\boldsymbol{s^\alpha}$ and $\boldsymbol{n^\alpha}$.

Note that even for crystals with modest numbers of slip systems, the number of partial differential equations to be solved can become large for the anisotropic crystal plasticity model. For example, for β-HMX, which consists of ten slip systems, the total number of equations is 87 for a full 3D simulation. Solving such large systems of equations with high-order schemes is computationally expensive. Therefore, we use high-order shock-capturing schemes for the hydrodynamic variables (ρ, u_i, E) and the coupling stresses (S_{ij}), while employing upwind schemes for advecting the SGS glide resistance, g_s^α and the lattice variables, viz., $\mathbf{s}^\alpha$, $\mathbf{n}^\alpha$ $\tilde{\boldsymbol{e}}_1$, and $\tilde{\boldsymbol{e}}_2$. This is based on the assumption that, under modest to strong shocks, the overall dynamics is governed by the hydrodynamic characteristics (i.e., the hyperbolicity is governed by the conservation laws for ρ, u_i, E, and S_{ij}), while g_s^α, $\mathbf{s}^\alpha$, $\mathbf{n}^\alpha$ $\tilde{\boldsymbol{e}}_1$, and $\tilde{\boldsymbol{e}}_2$ only follow the characteristics of ρ, u_i, E, and S_{ij}.

Furthermore, the shear strain-rates and the glide-resistances evolve under stiff source-terms [i.e., the right-hand sides of Eqs. (19) and (21) are power laws]. Therefore, all variables (S_{ij}, g_s^α, $\mathbf{s}^\alpha$, $\mathbf{n}^\alpha$ $\tilde{\boldsymbol{e}}_1$, $\tilde{\boldsymbol{e}}_2$), which are explicitly coupled to g_s^α are solved by an operator-splitting approach, i.e., by additively decomposing them into predicted values (S_{ij}^*, $g_s^{\alpha^*}$, $\mathbf{s}^{\alpha^*}$, $\mathbf{n}^{\alpha^*}$, $\tilde{\boldsymbol{e}}_1^*$, $\tilde{\boldsymbol{e}}_2^*$) followed by a correction update. In the predictor step, the variables are transported via the following equations:

$$\frac{\partial(\rho S_{ij}^*)}{\partial t} + (\rho u_k S_{ij}^*)_{,k} - \rho S_{ik}^* L_{kj} - \rho L_{ik} S_{kj}^* + \rho D_{kk} S_{ij}^* = \rho C_{ijkl} D_{kl} - \rho\left(\frac{1}{9} C_{kkll}\right) D_{pp}\delta_{ij}, \tag{24}$$

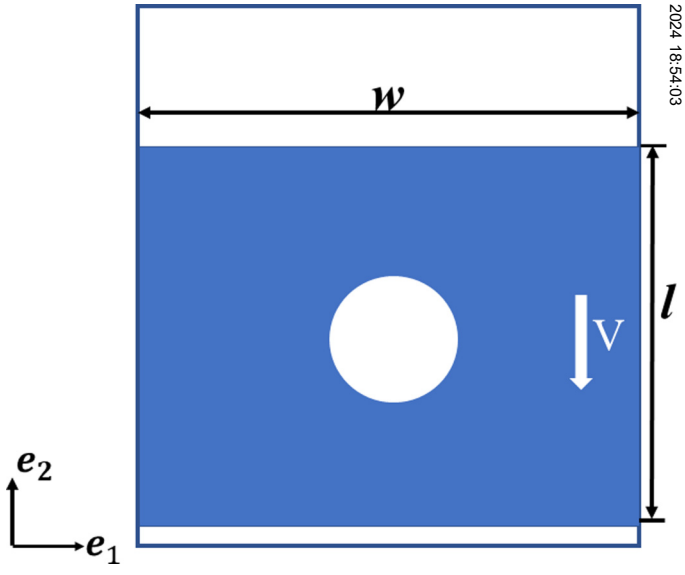

FIG. 3. Computational setup showing a block of a single-crystal β-HMX being impacted against the south domain boundary. The material contains a circular void of diameter D_{void}, whose center is at a distance of $l/2$ and $w/2$ from the bottom and the left surfaces of the block. The block is initialized with a uniform velocity of V m/s, directed toward $-\mathbf{e}_2$.

$$\frac{\partial(\rho\tilde{e}_{1i}^{*})}{\partial t}+(\rho u_j\tilde{e}_{1i}^{*})_{,j}=\rho L_{ij}\tilde{e}_{1j}^{*}, \tag{25}$$

$$\frac{\partial(\rho\tilde{e}_{2i}^{*})}{\partial t}+(\rho u_j\tilde{e}_{2i}^{*})_{,j}=-\rho L_{ji}\tilde{e}_{2j}^{*}, \tag{26a}$$

$$\frac{\partial(\rho s_i^{\alpha^*})}{\partial t}+(\rho u_j s_i^{\alpha^*})_{,j}=\rho L_{ij}s_j^{\alpha^*}, \tag{26b}$$

$$\frac{\partial(\rho n_i^{\alpha*})}{\partial t}+(\rho u_j n_j^{\alpha^*})_{,j}=-\rho L_{ji}n_j^{\alpha^*}, \tag{27a}$$

and

$$\frac{\partial(\rho g_s^{\alpha^*})}{\partial t}+(\rho u_j g_s^{\alpha^*})_{,j}=0. \tag{27b}$$

In the corrector step, the intermediate values of S_{ij}^{*}, $g_s^{\alpha^*}$, $\mathbf{s}^{\alpha^*}S$, $\mathbf{n}^{\alpha^*}$, $\tilde{\boldsymbol{e}}_1^{*}$, and $\tilde{\boldsymbol{e}}_2^{*}$ are updated via the following equations:

$$\frac{dS_{ij}}{dt}=-C_{ijkl}, \tag{28}$$

$$\frac{d\tilde{e}_{1i}}{dt}=-L_{ij}^{p^*}\tilde{e}_{1j}^{*}, \tag{29}$$

$$\frac{d\tilde{e}_{2i}}{dt}=L_{ji}^{p^*}\tilde{e}_{2j}^{*}, \tag{30a}$$

$$\frac{ds_i^{\alpha}}{dt}=-L_{ij}^{p^*}s_j^{\alpha^*}, \tag{30b}$$

$$\frac{dn_i^{\alpha}}{dt}=L_{ji}^{p^*}n_j^{\alpha^*}, \tag{31a}$$

and

$$\frac{dg_s^{\alpha}}{dt}=\sum_{\beta=1}^{n}h_{\alpha\beta}\left|1-\frac{g_s^{\beta^*}}{g_{sat}}\right|^{a}\operatorname{sign}\left(1-\frac{g_s^{\beta^*}}{g_{sat}}\right)\dot{\gamma}^{\beta^*}, \tag{31b}$$

where $L_{ij}^{p^*}=\sum_{\alpha=1}^{n}\dot{\gamma}^{\alpha^*}s_i^{\alpha^*}n_j^{\alpha^*}$ and $D_{ij}^{p^*}=0.5(L_{ij}^{p^*}+L_{ji}^{p^*})$. $\dot{\gamma}^{\alpha^*}$ is given by

$$\dot{\gamma}^{\alpha^*}=\min\left\{\dot{\gamma}^{0}\operatorname{sign}(\tau_s^{\alpha^*})\left|\frac{\tau_s^{\alpha^*}}{\tau_{th}^{\alpha^*}}\right|^{1/m},\quad \dot{\gamma}_0^{pd}\right\}, \tag{32}$$

where $\tau_s^{\alpha^*}=S_{ij}^{*}s_i^{\alpha^*}n_j^{\alpha^*}$ and $\tau_{th}^{\alpha^*}=r^{\alpha}g_s^{\alpha^*}$. The procedure for solving the entire set of equations is as follows:

(i) First, the direction cosines, (k_1, k_2, k_3), (m_1, m_2, m_3), and (n_1, n_2, n_3), computed from the current values of $\tilde{\boldsymbol{e}}_1$, $\tilde{\boldsymbol{e}}_2$, and $\tilde{\boldsymbol{e}}_3$, are used to calculate the transformation matrix $\mathbf{Q}$, using Eq. (14). This transformation matrix is used to compute the elastic constants C_{ijkl} in the current coordinate system, using the procedure described in Sec. II B.

(ii) The global conservation laws for mass, momentum, and energy [Eqs. (1)–(3)], and the predictor equation for the coupling stress [Eq. (24)] are solved to compute ρ, u_i, E, and S_{ij}^{*} at the current time step. To solve Eq. (24), the updated elastic constants C_{ijkl} of step (i) are used. The advection terms in these equations are spatially discretized using a third-order essentially non-oscillatory (ENO) scheme[47] and the fluxes are reconstructed using a local Lax–Friedrichs scheme,[48] while the spatial derivatives on the right hand-side in these equations are discretized using central differencing. These equations are integrated in time using a total variation diminishing third-order Runge–Kutta method.[50]

(iii) The pressure and the temperature are computed using the equation of state [Eqs. (5) and (6)] and Eq. (4), respectively, using the values of ρ, u_i, E calculated in step (ii).

(iv) The predictor equations for the SGS lattice variables and the slip-resistance [Eqs. (25)–(27)] are then solved to compute $g_s^{\alpha^*}$, $\mathbf{s}^{\alpha^*}$, $\mathbf{n}^{\alpha^*}$, $\tilde{\boldsymbol{e}}_1^{*}$, $\tilde{\boldsymbol{e}}_2^{*}$. The advection terms in the L.H.S. of these equations are spatially discretized using the first-order upwind scheme, while the velocity gradient terms on the right-hand side are discretized using central differences. The equations are integrated in time using a first-order forward Euler update.

(v) The SGS lattice variables and the slip resistances are corrected by solving Eqs. (28)–(31). These equations are solved by a semi-implicit stiff-equation solver using the computational package DVODE[51] to compute the updated values of S_{ij}, g_s^{α}, $\mathbf{s}^{\alpha}$, $\mathbf{n}^{\alpha}$ $\tilde{\boldsymbol{e}}_1$, $\tilde{\boldsymbol{e}}_2$.

(vi) The updated values of g_s^{α}, $\mathbf{s}^{\alpha}$, $\mathbf{n}^{\alpha}$ are used to compute the plastic strain-rate, $\dot{\gamma}^{\alpha}$ using Eq. (19), which, in turn, is used to compute the plastic-strain rate tensor, D_{ij}^{p} using Eq. (9).

In the above solution strategy, it is assumed that the characteristics of the system are dominated by the shock hydrodynamics. Therefore, the stress evolution is solved using an operator splitting approach, where the elastic stresses are only updated in step (v) by a semi-implicit solve. For a more general setting, the shear rates may need to be fully coupled with the stress evolution. The above steps are repeated at every time instant to march the flow variables ρ, u_i, E, p, T, S_{ij}, as well as the SGS variables, g_s^{α}, $\mathbf{s}^{\alpha}$, $\mathbf{n}^{\alpha}$ $\tilde{\boldsymbol{e}}_1$, $\tilde{\boldsymbol{e}}_2$ forward in time. For delineating voids and multiple materials embedded in the flow field, a narrow-band levelset[52] method is used; this allows for tracking the material interfaces in a sharp manner. Once the interfaces are identified by the zero levelset contours, the interfacial boundary conditions are applied using a variant of the ghost fluid method (GFM).[53] Detailed descriptions of the levelset and ghost-fluid methods are provided in our previous works[22,23,32,35,54] and are not repeated here for brevity.

III. RESULTS AND DISCUSSION

The methods presented in Sec. II are used to perform 2D (plane strain) simulations of the response of a single crystal β-HMX material subject to shock loading. The glide directions and the unit normals of the slip systems for the material are given in Table I. Amore detailed description of the crystal system provided in previous works,[3,6] where the model was originally developed and

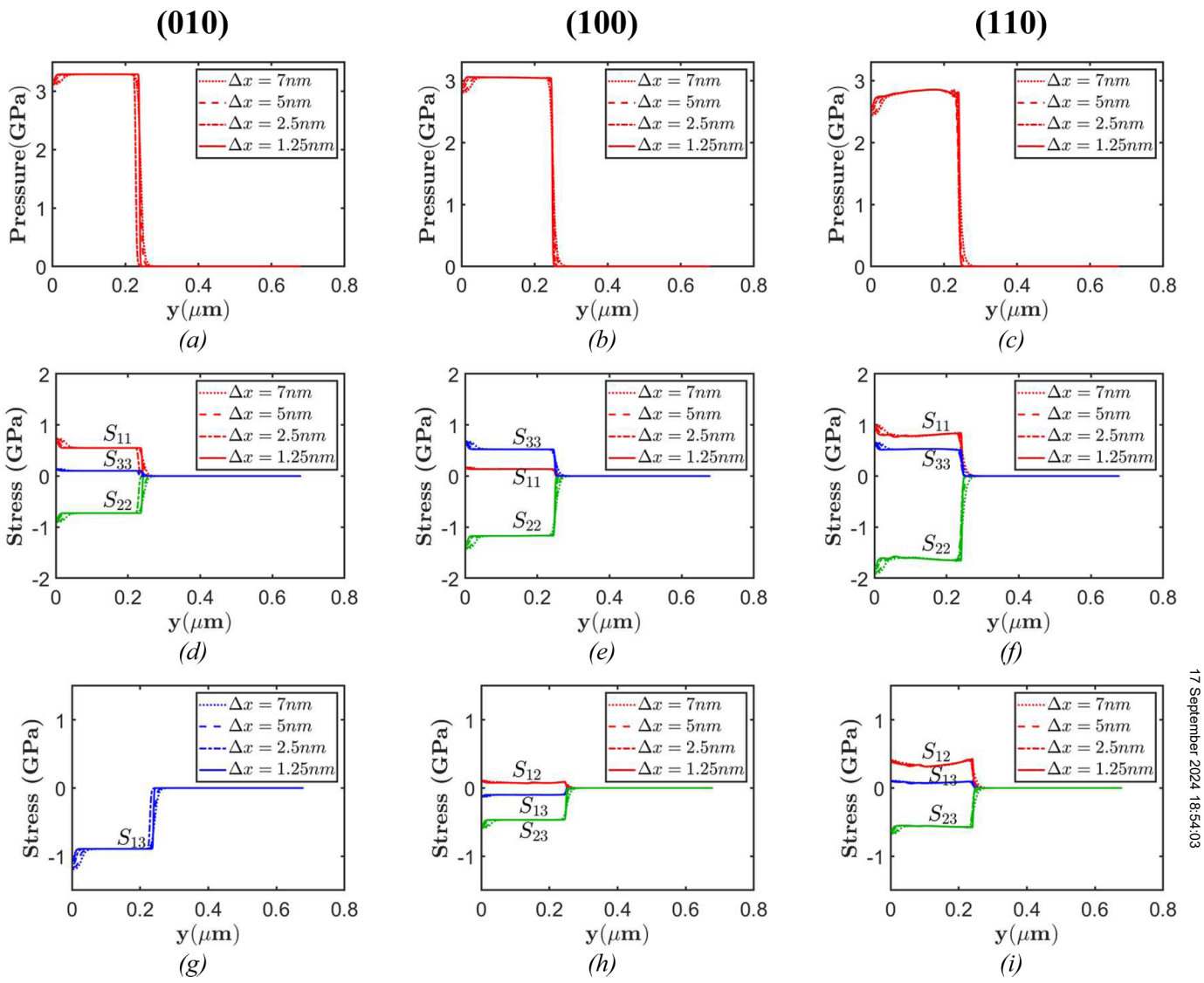

FIG. 4. Grid refinement study showing the effect of mesh-sizes on the pressure [Figs. (a)–(c)], normal components of $\boldsymbol{S}_{ij}$ [Figs. (d)–(f)], and the shear components of $\boldsymbol{S}_{ij}$ [Figs. (g)–(i)] at 60 ps after an impact for a purely elastic void-free HMX material subjected to a velocity of 500 m/s. The first column [(a), (d), and (g)] is for a shock traveling normal to (010), the second column [(b), (e), and (h)] is for a shock traveling normal to (100), while the third column [Figs. (c), (f), and (i)] is for a shock traveling normal to (110). In Fig. (g), $\boldsymbol{S}_{12}$ and $\boldsymbol{S}_{23}$ are not shown, as they are zero.

validated. Table II lists the non-zero elastic constants and the values of other material parameters required for simulating the shock-response of β-HMX.[6,19] The computational framework described in this paper is used to first perform grid refinement studies on a shocked purely elastic sample of β-HMX (Sec. III A). Following this, we compare the individual stress components from the Eulerian computational models with the Lagrangian model. We benchmark our computations using the full elastoplastic model presented in the preceding section, comparing both the individual stress components as well as the resolved shear stresses on individual slip planes. After benchmarking the Eulerian computations and establishing confidence that the calculations of the current framework are reliable, we then validate the complete elastoplastic predictions of the current Eulerian framework against MD-computed Hugoniotstat data[19] as well as the experimental Hugoniot reported in Menikoff and Sewell.[34] These studies seek to show that the current Eulerian framework satisfies the essential physics of β-HMX under shock loading. Shock-induced collapse of a micrometer-sized void, i.e., of a size typically encountered in microstructures of energetic materials is then simulated for

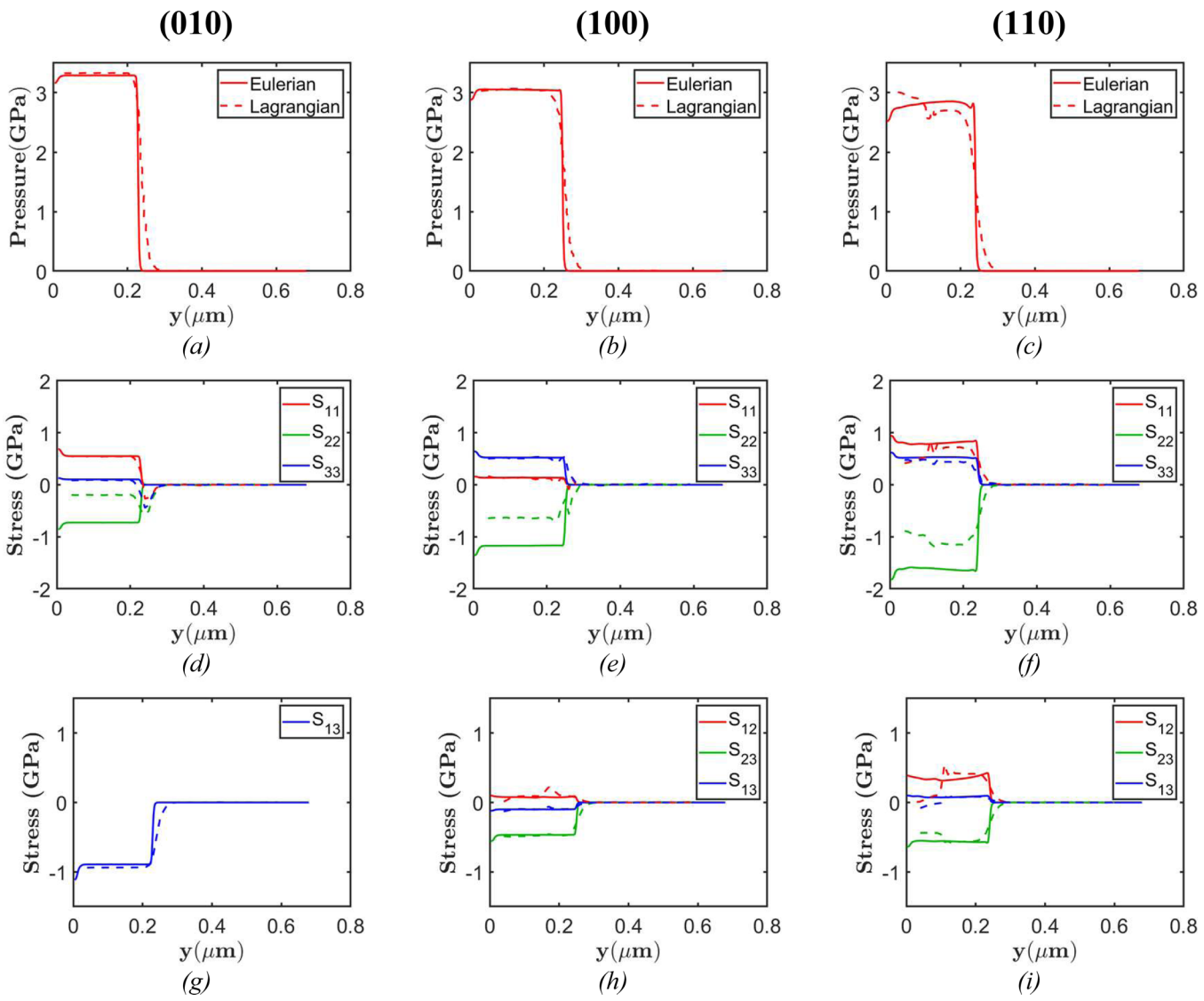

FIG. 5. Comparison of the stresses and the thermodynamic pressure between the current Eulerian formulation and the Lagrangian formulation. The plots compare the pressure [Figs. (a)–(c)], normal components of $\boldsymbol{S}_{ij}$ [Figs. (d)–(f)], and the shear components of $\boldsymbol{S}_{ij}$ [Figs. (g)–(i)] at 60 ps after the impact for a purely elastic void-free HMX material subjected to a velocity of 500 m/s. The first column [(a), (d), and (g)] is for a shock traveling normal to (010), the second column [(b), (e), and (h)] is for a shock traveling normal to (100), while the third column [Figs. (c), (f), and (i)] is for a shock traveling normal to (110). In Fig. (g), $\boldsymbol{S}_{12}$ and $\boldsymbol{S}_{23}$ are not shown, as they are zero. The solid lines show the computations of the Eulerian formulation, while the dotted lines show the computations of the Lagrangian formulation.

different impact velocities to investigate the effect of anisotropy on hotspot formation. The void size studied in this work is significantly larger than the nano-scale voids that are typically simulated in MD calculations. This is because, as discussed in Refs. 55, 56, voids smaller than 0.1 μm are rather sparse in real HMX samples and do not contribute significantly to the global porosity of the material. Furthermore,[11,57,58] the hotspots produced by nano-sized voids are easily quenched by thermal diffusion and are unlikely to contribute to the shock sensitivity of β-HMX.

The computational setup for performing shock simulations is shown in Fig. 3. The setup comprises a patch of solid β-HMX with dimensions w and d in $\boldsymbol{e}_1$ and $\boldsymbol{e}_2$ directions, respectively; for void collapse simulations, a circular void of diameter, $D_{void} = 0.5\,\mu$m, is inscribed within the patch with its center coincident with the centroid of the block, as shown in the figure. The void and the patch of material in the computational setup are delineated by levelsets and embedded inside the overall computational domain. The computational domain outside the levelset defining the patch is

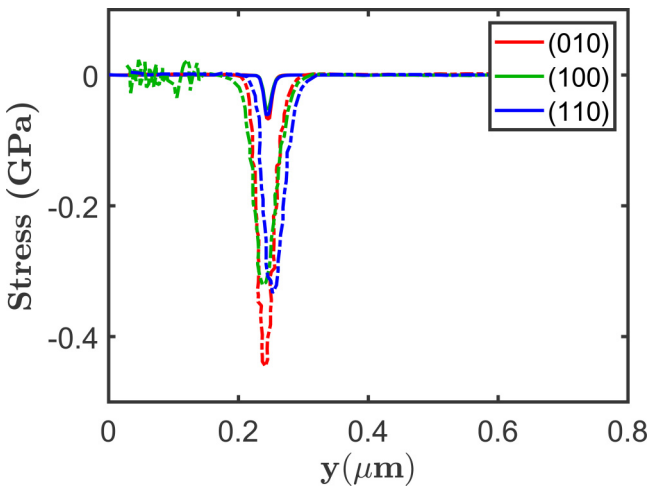

FIG. 6. Artificial viscous stresses at 60 ps after a 1-D impact for a purely elastic HMX material subjected to a velocity of 500 m/s. The solid lines show the addi-tiional artificial viscous stress in the material used in the Eulerian computations, while the dashed lines show the push-forward of the artificial viscous stresses used in the Lagrangian computations. For the purpose of brevity, only the two–two component of the artificial viscous stress tensors is shown.

modeled as vacuum, and reflective boundary conditions are applied at all edges. To initiate a shock in the material, a reverse-ballistic setup is simulated, i.e., the material is prescribed a uniform downward velocity of V at $t = 0$ and impacts the south boundary of the domain. Reflective boundary conditions at the south boundary mimic a stationary rigid piston, i.e., once the material is in contact with the boundary, the rigid translation of the material is arrested and a shock wave is initiated in the positive $\boldsymbol{e}_2$ direction. The material is oriented such that the normal to the loading plane is parallel to the $\boldsymbol{e}_2$ direction; all computations in this paper are performed for three different loading directions, i.e., the impact is normal to the planes (010), (100) , or (110).

A. Grid refinement studies

To study the effect of numerical approximations induced by the grid size employed, we first set $\dot{\gamma}_0^{pd}$ to 0 and obtain the solutions for a pure elastic anisotropic material model. This allows for ascertaining the influence of numerical viscosity on the shock dynamics of the material. The propagation of a planar shock in a void-free block of β-HMX is simulated; the setup is as in Fig. 3, with w and d set to 0.4 and 0.65 μm, respectively, and D_{void} set to 0. Computations are performed for an impact velocity $V = 500$ m/s, and the solutions at time instant $t = 64$ ps are compared at $x = 0.2\,\mu$m for three different grid sizes, $\Delta x = \Delta y = 7$, 5, 2.5, and 1.25 nm.

Figure 4 shows the comparison of the pressure and stress fields, p and S_{ij}, respectively, for the different grid sizes. Convergence of the solutions with improved resolution is observed. As expected, the figure shows that the jumps in the calculated quantities become steeper as the mesh resolution increases. In addition to monotonic convergence, Fig. 4 also shows the effects of loading direction on p and S_{ij}. The magnitude of pressure is the highest for the (010) direction in Fig. 4(a) and the lowest for the (110) direction in Fig. 4(c), while the normal stress in the shock propagation direction, S_{22}, shows the opposite trend. It is lowest for the (010) direction and the highest for the (110) direction. Figures 4(d) and 4(e) also show that the transverse normal stress, S_{11}, is negligibly small for the (100) direction and is the highest for the (110) direction. However, the out-of-plane stress, S_{33}, is negligible for the (010) direction and comparable for the other two loading directions. With regard to shear stresses, it is observed that all three components are non-zero for the (100) and (110) directions, as seen is Figs. 4(h) and 4(i), while only S_{13} is non-zero for the (010) direction. This is due to the monoclinicity of the β-HMX crystal. Since the impact velocity V and, consequently, the shock propagation direction is parallel to $\boldsymbol{e}_2$ and D_{22} is the only non-zero component of the strain-rate tensor. From Eq. (7), it follows that for S_{23}, S_{13}, and S_{12} to be non-zero, the corresponding elastic constants $\mathbb{C}_{24}$, $\mathbb{C}_{25}$, and $\mathbb{C}_{26}$ must also be non-zero. However, due to the monoclinicity of the crystal, it can be shown that for the (010) direction, $\mathbb{C}_{25} = \tilde{\mathbb{C}}_{25} = 6.81$ GPa, while $\mathbb{C}_{24} = \tilde{\mathbb{C}}_{24} = 0$ and $\mathbb{C}_{26} = \tilde{\mathbb{C}}_{26} = 0$. Therefore, S_{13} is the only non-zero shear component in Fig. 4(g). It can further be verified that for the (100) and the (110) directions, all three components, viz., $\mathbb{C}_{24}$, $\mathbb{C}_{25}$, and $\mathbb{C}_{26}$ are non-zero, with $\mathbb{C}_{25}$ having the smallest value. Therefore, in Figs. 4(h) and 4(i), all the three shear stresses are non-zero, with S_{13} being the lowest shear-stress component. Thus, different shear stress components are activated due to the monoclinicity of the crystal for different loading directions.

Finally, Fig. 4 provides verification that the components of S_{ij} are in the same ratio as the corresponding elastic constants. For example, for the (010) direction, Figs. 4(d) and 4(g) show that the ratio of the stress components S_{11}:S_{22}:S_{33}:S_{13} follows the ratio $(\mathbb{C}_{12} - K_0)$:$(\mathbb{C}_{22} - K_0)$:$(\mathbb{C}_{23} - K_0)$:$\mathbb{C}_{25} = 0.5$: -0.79: 0.1: -0.85. These ratios are consistent with Eq. (7) for the case where the impact velocity V is parallel to the $\boldsymbol{e}_2$ direction (i.e., when D_{22} is the only non-zero component of the strain-rate tensor). Thus, the above grid refinement study demonstrates that the current Eulerian implementation provides grid independent computation of shock propagation in the anisotropic β-HMX crystal and captures the distribution of stresses expected due to the crystalline orientation relative to the shock direction. Based on this grid refinement study, to balance the computational cost and discretization errors, a grid size of $\Delta x = \Delta y = 2.5$ nm is adopted in further computations unless otherwise mentioned. Further benchmarking of the Eulerian computational model is presented in Sec. III B.

B. Benchmarking and validation

1. Shock propagation in an anisotropic elastic material —Comparison with Lagrangian simulations

Calculations performed with the present Eulerian framework are compared to Lagrangian calculations under identical shock loading conditions. First, we examine the stresses developed along relevant crystalline orientations, focusing on the shock response of a pure elastic β-HMX material by setting $\dot{\gamma}_0^{pd}$ to 0. The sample shown in Fig. 3 is loaded along three different directions to test the

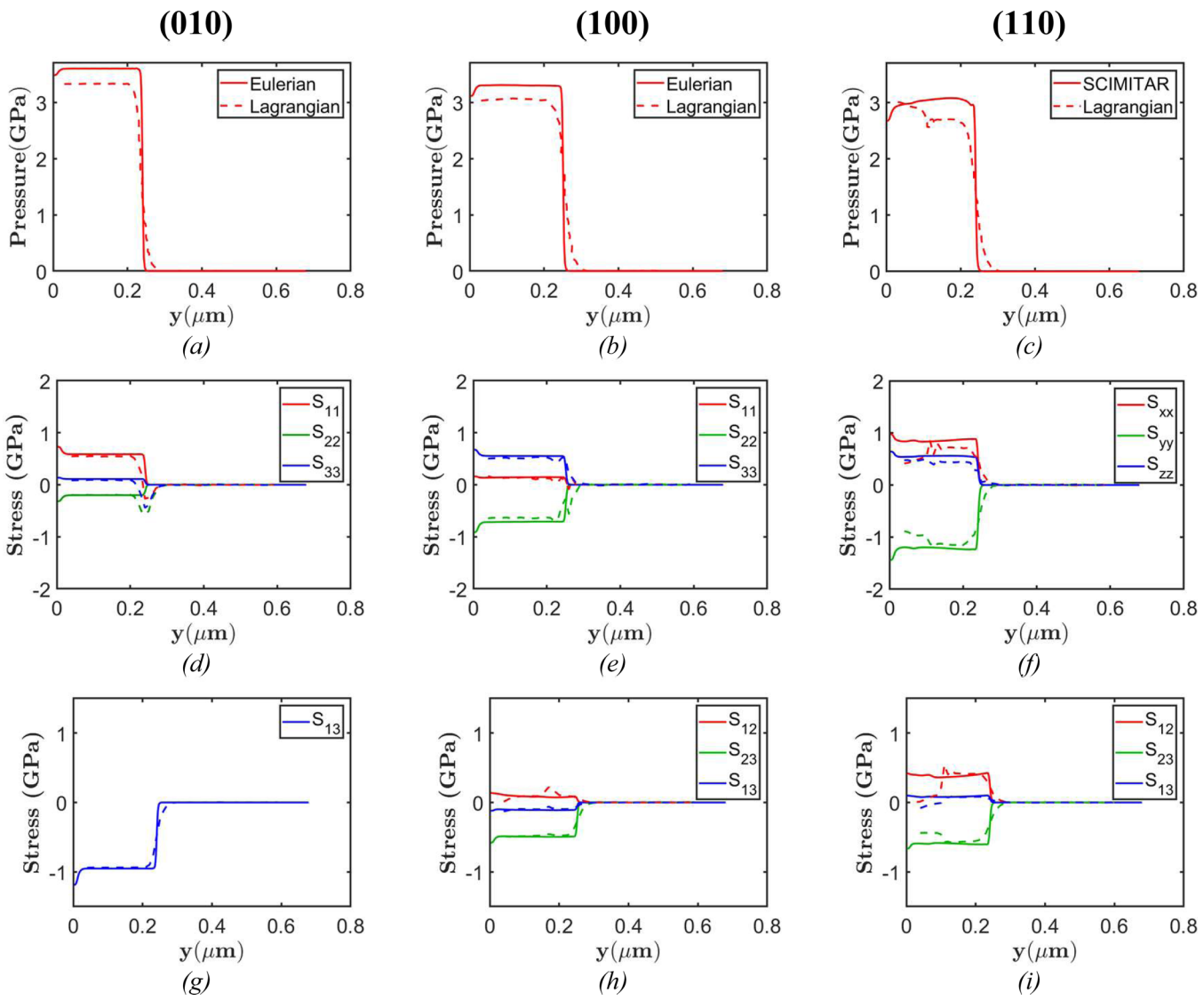

FIG. 7. Comparison of the stresses and the thermodynamic pressure between the current Eulerian formulation using the artificial viscosity and the Lagrangian formulation. The plots compare the pressure [Figs. (a)–(c)], normal components of $\boldsymbol{S}_{ij}$ [Figs. (d)–(f)], and the shear components of $\boldsymbol{S}_{ij}$ [Figs. (g)–(i)] at 60 ps after the impact for a purely elastic void-free HMX material subjected to a velocity of 500 m/s. The first column [(a), (d), and (g)] is for a shock traveling normal to (010), the second column [(b), (e), and (h)] is for a shock traveling normal to (100), while the third column [(c), (f), and (i)] is for a shock traveling normal to (110). In Fig. (g), $\boldsymbol{S}_{12}$ and $\boldsymbol{S}_{23}$ are not shown as they are zero. The solid lines show the Eulerian computations, while the dotted lines show the computations of the Lagrangian formulation.

ability of the Eulerian model to accurately calculate orientational effects on the stress field. Figure 5 shows the comparison of the calculated pressure p and deviatoric stress component S_{ij} between the Eulerian and the Lagrangian computations. Several observations can be made from Fig. 5 as described below.

First, it can be noted that the shock locations for all the three loading directions are in good agreement between the Eulerian and the Lagrangian computations. The observed difference between the two computational models is in the resolution of the shock front. As seen in Fig. 5(a), the jump in pressure across the shock is captured sharply in the Eulerian computation, while the discontinuity is distributed over a larger spatial extent in the Lagrangian computation. This is because the Lagrangian computation spreads the shock over a few elements due to the use of an artificial viscous stress, where the first viscosity coefficient C_0 in Eq. (33) controls the thickness of the shock front. In contrast, the present Eulerian computations discretize the governing equations using a shock-capturing scheme (ENO), which ensures that the entropy condition

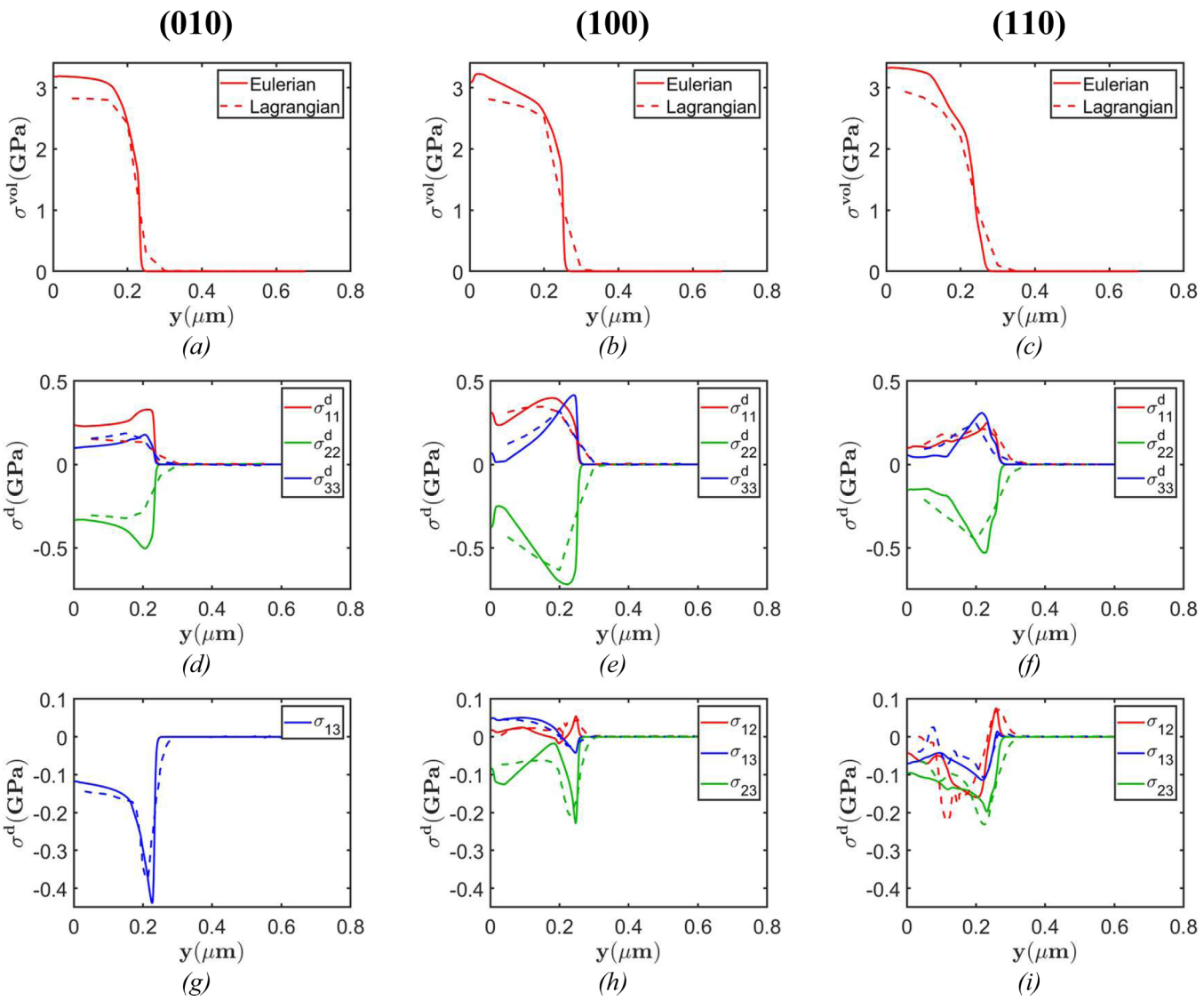

FIG. 8. Comparison of the volumetric and the components of the deviatoric stresses between the current Eulerian formulation and the Lagrangian formulation. The plots compare the volumetric stress, $\boldsymbol{\sigma}^{vol}$, [Figs. (a)–(c)], normal components of the deviatoric stresses, $\boldsymbol{\sigma}^{d}$, [Figs. (d)–(f)], and the shear components of the deviatoric stresses, $\boldsymbol{\sigma}^{d}$ [Figs. (g)–(i)] at 60 ps after the impact for an elastoplastic void-free HMX material subjected to a velocity of 500 m/s. The first column [(a), (d), and (g)] is for a shock traveling normal to (010), the second column [(b), (e), and (h)] is for a shock traveling normal to (100), while the third column [(c), (f), and (i)] is for a shock traveling normal to (110). In Fig. (g), 12 and 23 components of $\boldsymbol{\sigma}^{d}$ are not shown as they are zero. The solid lines show the Eulerian computations, while the dotted lines show the computations of the Lagrangian formulation.

is satisfied and therefore explicit artificial viscosity is not required. Thus, the difference in resolution of the shock-fronts between the Eulerian and the Lagrangian computations, which can be observed for all the three loading directions in Fig. 5, results from the differences in numerical schemes employed to capture shocks in these frameworks.

Second, Fig. 5 shows that the transition from the unshocked to the post-shocked state is monotonic in the Eulerian computations for the pressure p as well as all components of S_{ij} and for all the loading directions. However, in the Lagrangian calculations, the post-shocked p, S_{11}, and S_{12} show small oscillations for the (110) loading direction [Figs. 5(c), 5(f), and 5(i)], while a few stress components manifest an initial dip, followed by a rise for the (010) and (100) directions. This is observed in S_{11}, S_{22}, and S_{33} in Fig. 5(d) and in S_{22} in Fig. 5(e). Since the Eulerian computations use shock capturing schemes with inbuilt viscosity solutions, these

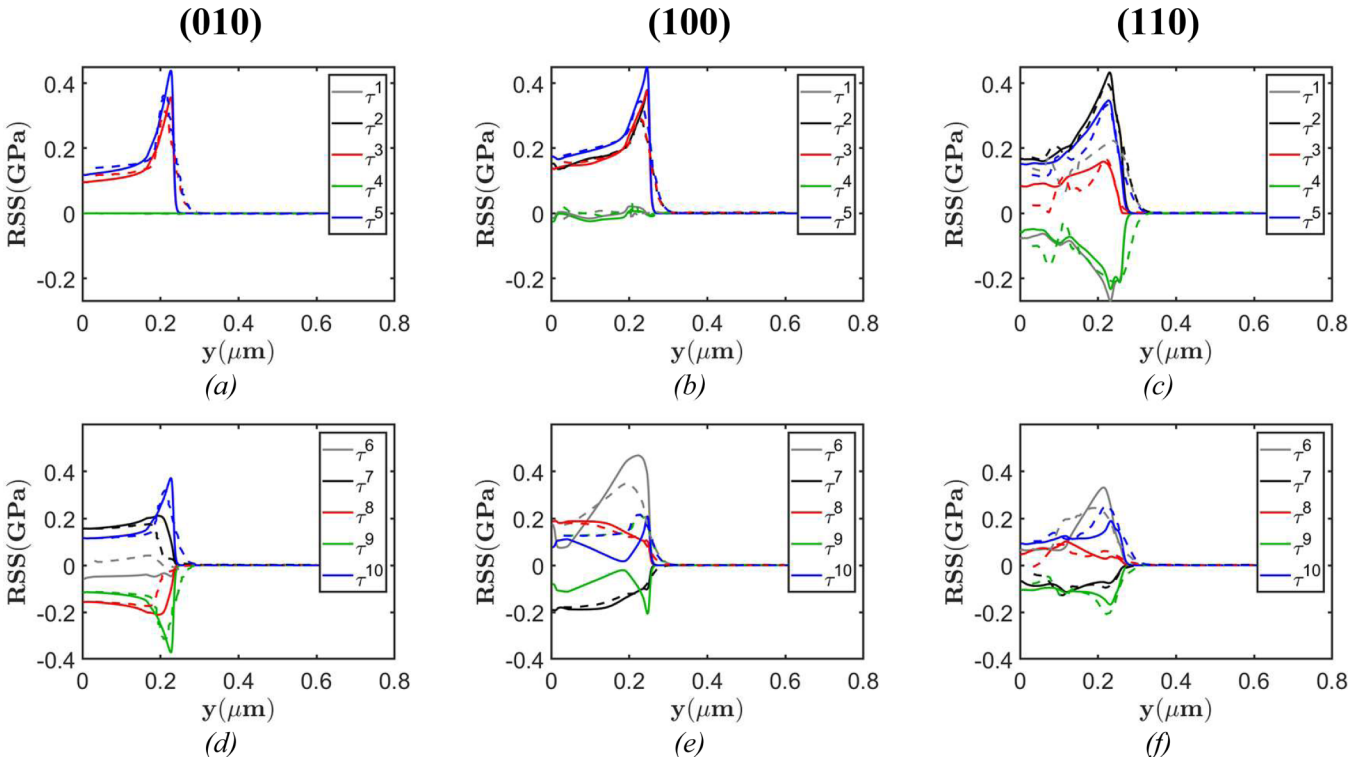

FIG. 9. Comparison of the individual resolved sheared stresses (RSS) between the current Eulerian formulation and the Lagrangian formulation. Figures (a)–(c) compare the RSS for the first five slip systems, while Figs. (d)–(f) compare the RSS for the last five slip systems, as compared at 60 ps after the impact for an elastoplastic void-free HMX material subjected to a velocity of 500 m/s. The first column [(a) and (d)] is for a shock traveling normal to (010), the second column [(b) and (e)] is for a shock traveling normal to (100), while the third column [Figs. (c) and (f)] is for a shock traveling normal to (110). The solid lines show the Eulerian computations, while the dotted lines show the computations of the Lagrangian formulation.

oscillations or non-monotonicity are not present in the post-shocked p and S_{ij} Eulerian results in Fig. 5. The oscillations and non-monotonicity are also due to the artificial viscous stresses and has been observed in other works (see Noh[59]). Calibration of the viscosity coefficients to tune the amount of shock-front diffusion supplied to suppress spurious oscillations may obviate the non-monotonicity through the shock zones. Such calibration is challenging to perform for a general anisotropic field and for a wide range of shock loading intensities.

Finally, Fig. 5 shows that the magnitudes of the post-shocked pressure p, shear stresses (S_{12}, S_{23}, and S_{13}), and the transverse and the out-of-plane components of the normal coupling stresses (S_{11} and S_{33}) are in good agreement between the Lagrangian and the Eulerian computations. However, the normal coupling stress in the direction of shock propagation, S_{22}, is somewhat higher in the Eulerian computation, compared to the Lagrangian solutions. Closer examination shows that in the Lagrangian computations, the ratios of the stresses, S_{11}:S_{22}:S_{33}:S_{13}, are considerably different from the ratio of the elastic constants, $(\mathbb{C}_{12} - K_0)$:$(\mathbb{C}_{22} - K_0)$:$(\mathbb{C}_{23} - K_0)$:$\mathbb{C}_{25}$. It has been verified for the (010) loading direction that this difference in ratios is not due to push forward of the PK2 stresses, as both the Jacobian and the non-zero component of the deformation gradient, F_{22}, are of order 1 ($O \sim 0.87 - 0.9$) in the pull-back operation, $\boldsymbol{JF}^{-1}\boldsymbol{SF}^{-T}$; this verification is not presented here for the sake of brevity. We hypothesize that this disagreement arises due to the difference in the decomposition of the stress tensor between the Lagrangian and the Eulerian computations. In the Eulerian framework, the stress tensor is comprised of the pressure and the coupling stresses, whereas in the Lagrangian framework, an artificial viscous stress is used in addition to the pressure and the coupling stress. Figure 6 shows $\mathbf{P}^{\text{viscous}}$ in the Lagrangian computations for the different loading directions, with the value of the transient viscous stress $\sim O(0.5\,\text{GPa})$ near the shock front. Comparison of Fig. 6 with Figs. 5(d)–5(f) shows that this artificial viscous stress is comparable in magnitude to the post-shocked coupling stresses S_{22} in the Lagrangian computations. This implies that a significant component of the imparted momentum is partitioned into the viscous stresses, at least near the shock front. This additional viscous dissipation near the shock front is absent in the post-shock S_{22} in the Eulerian computational framework; therefore, the post-shock S_{22} is higher in the Eulerian computations. Additionally, we note that in the present Eulerian calculations the components of stresses are in the same ratio as the elastic constants, indicating a physically correct evaluation of the stresses along the different orientations.

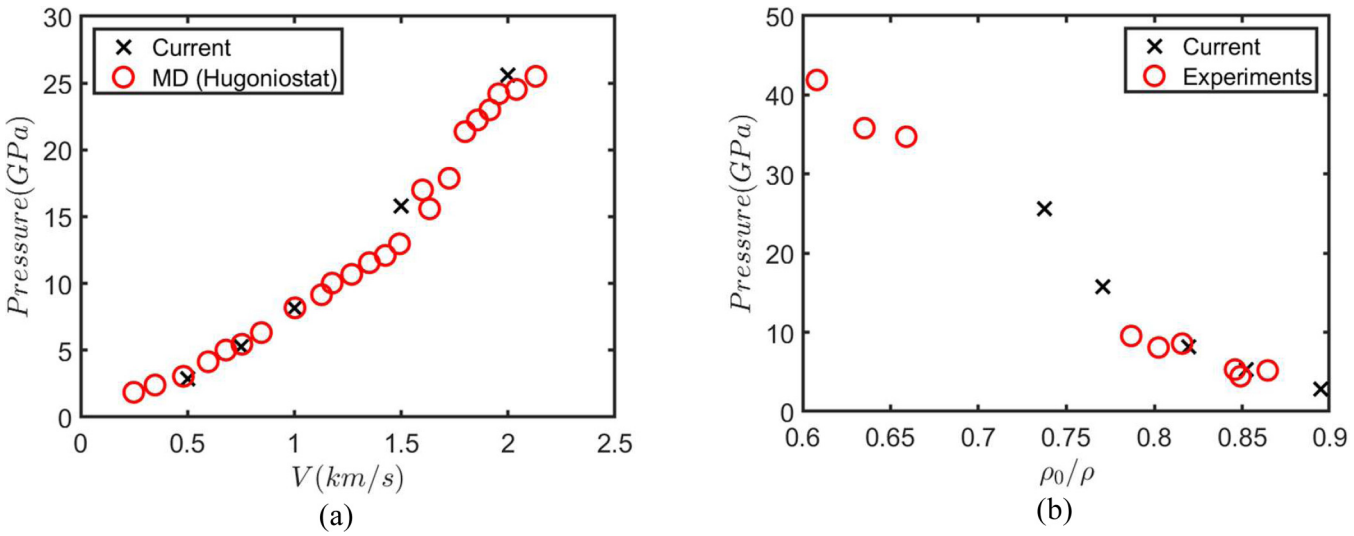

FIG. 10. Comparison of the (a) pressure-particle velocity variation behind the shock between the current Eulerian computations and the MD Hugoniotstat data as reported in Ref. 30, and (b) the pressure and the compression–ratio relation behind the shock between the Eulerian computations and the experimental data as reported in Ref. 33. In the Eulerian computations, the void-free $\boldsymbol{\beta - HMX}$ specimen described in Fig. 3 is loaded in a reverse-ballistic configuration in the (010) direction. The loading velocities are 500, 750, 1000, 1500, and 2000 m/s.

To evaluate the above hypothesis regarding the causes underlying the differences in the ratio of stresses between the Lagrangian and Eulerian calculations, a small viscous stress was purposefully added to the coupling stresses in the Eulerian formulation. Thus, the Cauchy stress tensor, σ_{ij}, was decomposed additively as, $\sigma_{ij} = -p\delta_{ij} + S_{ij}$, where an additional viscous stress was explicitly added in the Eulerian framework, of the same form as the artificial viscous stress in the Lagrangian case, viz.,[60]

$$S_{ij}^{viscous} = [C_2 c_0 \Delta x + C_3 |D_{kk}| (\Delta x)^2] D_{ij}, \tag{33}$$

where C_2 and C_3 are viscosity coefficients, whose values are given in Table II. The key question that underpinned the addition of $S_{ij}^{viscous}$ in the Eulerian system was the following: Do *all* components of the stress tensor of the Lagrangian and the Eulerian computations agree if an appropriate amount of additional dissipation is added to the Eulerian system? Note that the values of C_2 and C_3 are chosen to be smaller than the values of the Lagrangian viscosity coefficients, C_0 and C_1. This is because these coefficients in the Lagrangian computation are calibrated to prevent spurious oscillations near the shock front. However, in the Eulerian computations, the ENO scheme already satisfies entropy conditions and prevents oscillations near the shock-front by construction. Therefore, only a small amount of additional artificial viscous stresses is added in the Eulerian computations with the express purpose of emulating the dissipation of the Lagrangian computational system. The simulations for shock propagation in a pure elastic β-HMX material are then repeated for the same computational setup as before. Figure 6 shows the stress component containing the viscous contribution $S_{22}^{viscous}$ for the three loading directions in the Eulerian computations. Note that $S_{22}^{viscous}$ is small compared to the push-forward of the Lagrangian stress $\mathbf{P}^{\mathbf{viscous}}$. This is expected because $\mathbf{P}^{\mathbf{viscous}}$ is the total viscous dissipation demanded by the Lagrangian computations to suppress oscillations near the shock-front, whereas $S_{22}^{viscous}$ only reflects the additional viscosity artificially added in the Eulerian system via Eq. (33).

Figure 7 compares the components of p and S_{ij} between the Lagrangian and the Eulerian computations with the added artificial viscous stress. The figure shows that with the additional viscosity in the Eulerian system, all components of S_{ij} agree well between the Eulerian and the Lagrangian computations. The pressure is slightly higher in Figs. 7(a)–7(c) in comparison to the Lagrangian computations as well as in comparison to the previous Eulerian computations without the additional viscosity [Figs. 5(a)–5(c)]. Therefore, with the added dissipation in the Eulerian system, the elastic solutions of the current Eulerian formulation are in better agreement for all stress components with the Lagrangian computations. Therefore, the differences between the present Eulerian and the Lagrangian calculations can be attributed to the application of explicit artificial viscous terms in the latter approach.

It is noted that an artificial viscosity is not required in the current Eulerian framework and was only added for the discussion of Fig. 7 to examine the effect of the additional dissipation applied in the Lagrangian computations. Since an entropy satisfying shock-capturing scheme is used in the present Eulerian framework, the artificial viscous stresses of Eq. (33) will not be retained in the definition of S_{ij} for the remainder of the paper.

2. Comparison of shock propagation in an elastoplastic material

In Sec. III B 1, the purely elastic material model was employed to compare results between the present approach and a traditional

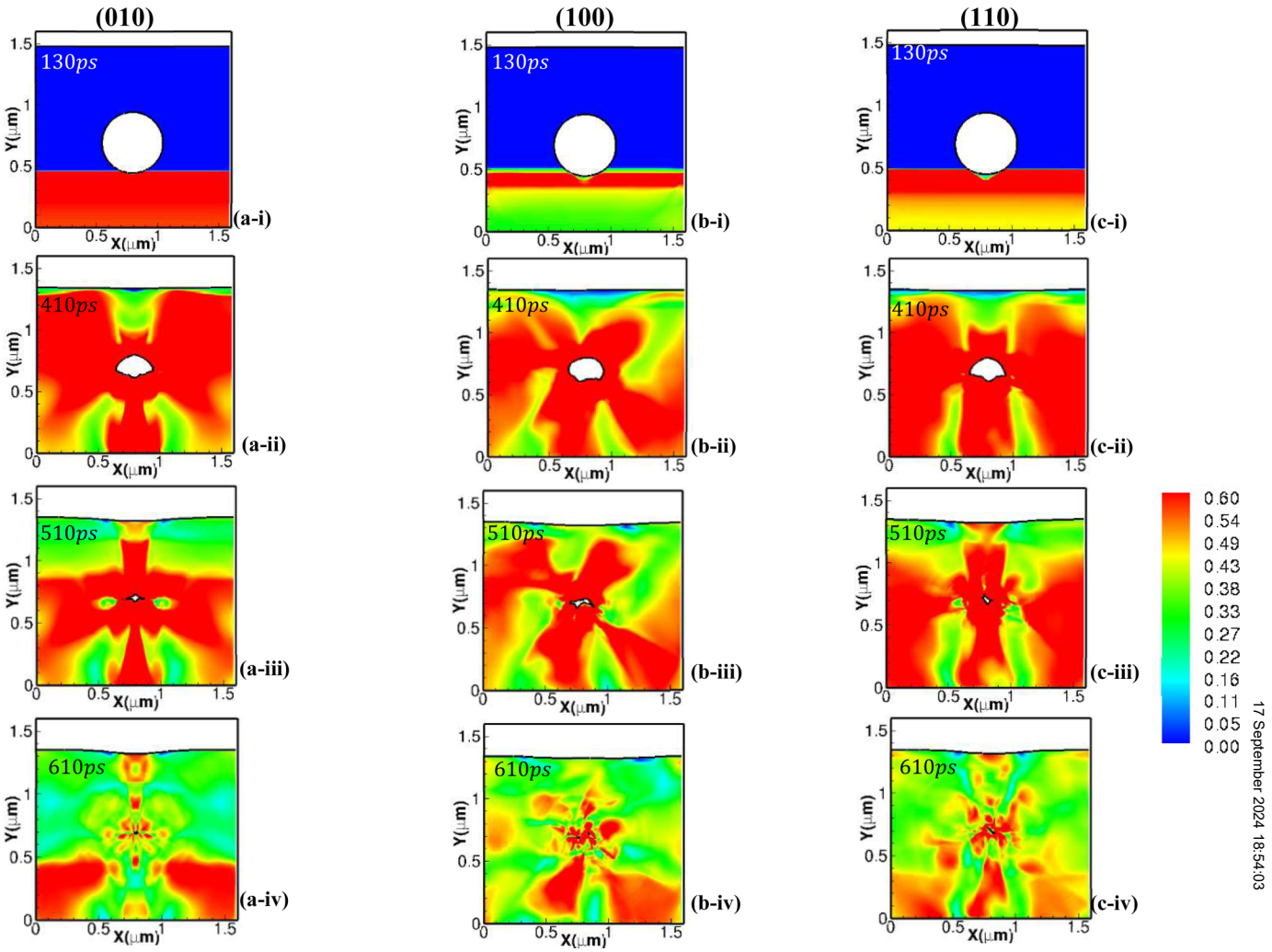

FIG. 11. Evolution of the von Mises stress in GPa at different time-instances during the collapse of a void of diameter 0.5 μm due to a reverse-ballistically induced impact velocity of 500 m/s. The three columns show the contours of the von Mises stresses for the shock directed normal to the (100), (010), and (110) planes for HMX.

Lagrangian formulation. The two methods are now compared for an elastoplastic material, i.e., the constraint $\dot{\gamma}_0^{pd} = 0$ is removed; instead, the value shown in Table II is prescribed. Similar to the cases in Secs. III A and III B 1, computations are performed for $V = 500$ m/s, and the solutions at $t = 64$ ps are compared at $x = 0.2\,\mu$m. Comparisons between the Eulerian and the Lagrangian computations are shown with respect to the volumetric stresses, $\sigma^{vol} = -p + S_{kk}/3$, and the components of the deviatoric stresses, $\sigma_{ij}^{d} = S_{ij} - \frac{1}{3}S_{kk}\delta_{ij}$.

Figure 8 shows comparisons of the calculated stress components for the three loading directions, (010), (100), and (110). Figure 8(a) through 8(c) show that for all three loading directions, σ^{vol} is slightly higher in the Eulerian computations, in comparison to the Lagrangian values. Similar observations are also made in Fig. 8(d) through 8(f), where the normal components of the deviatoric stresses are seen to be slightly higher in the Eulerian computations. With regard to the shear stresses, with the exception of minor oscillations in the Lagrangian solutions of σ_{12}^{d} and σ_{13}^{d} for the (110) loading direction [Fig. 8(i)], the Eulerian computations are in good agreement with the Lagrangian case. Furthermore, the plastic relaxation of the deviatoric stresses is also seen to be in reasonable agreement between the Lagrangian and the Eulerian computations. For instance, in Fig. 8(e), both the Lagrangian and the Eulerian simulations show that the normal components of σ_{ij}^{d} peak at the shock front followed by a decay behind the shock. The spatial extent of the post-shock relaxation zones is also in good agreement between the two approaches. Thus, Fig. 8 shows that the stresses from the elastoplastic Eulerian computations agree well

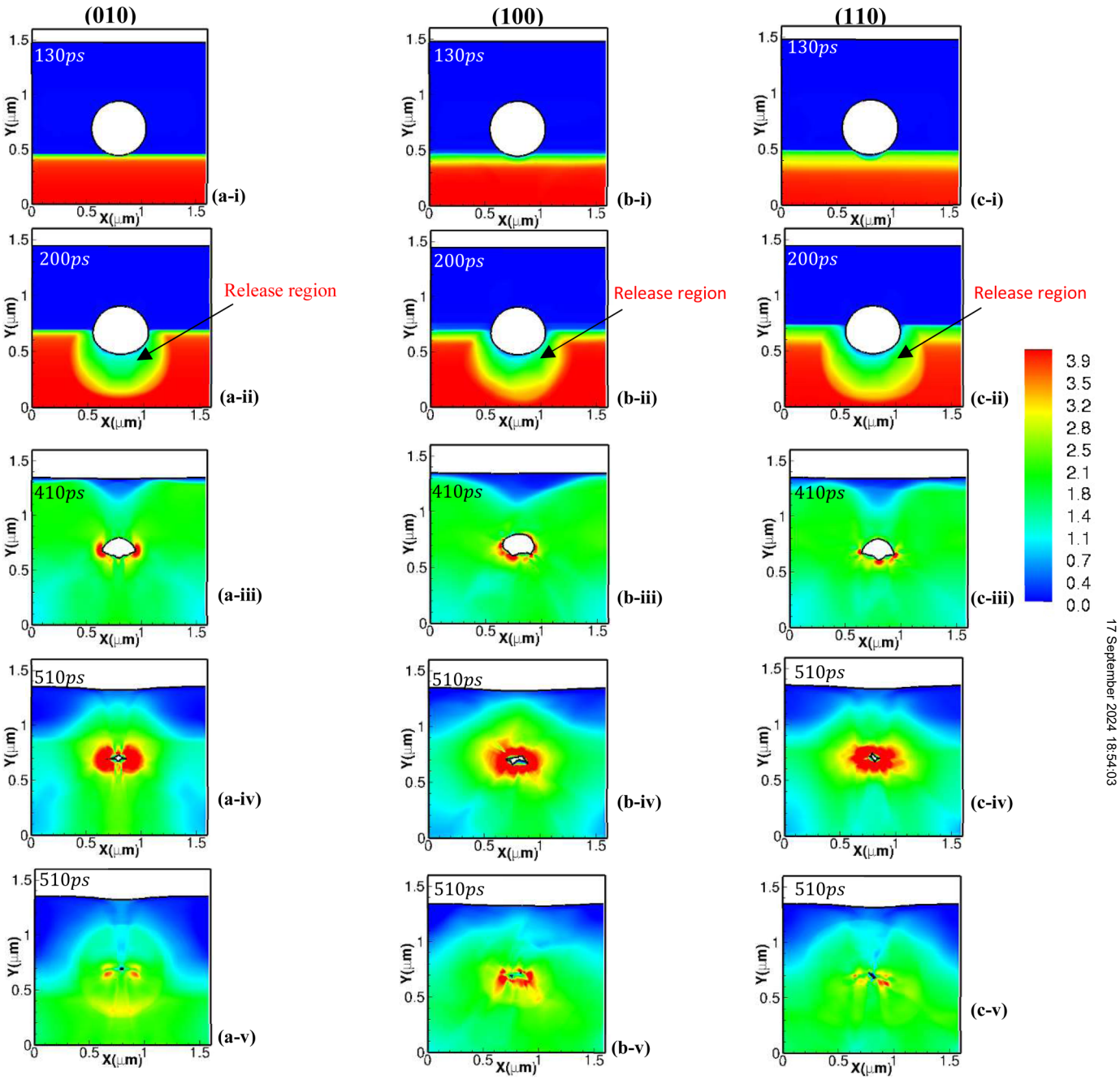

FIG. 12. Evolution of the pressure in GPa at different time-instances during the collapse of a void of diameter 0.5 μm due to a reverse-ballistically induced impact velocity of 500 m/s. The three columns show the contours of the pressure for the shock directed normal to the (100), (010), and (110) planes for HMX.

with those from the Lagrangian simulations, despite the use of an artificial viscosity in the latter approach.

In addition to the components of the Cauchy stresses, the resolved shear stresses, τ^{α}, on the different slip-systems are compared between the Lagrangian and the Eulerian computations. Figure 9 shows the comparisons of τ^{α} for the three loading directions. The values of τ^{α} are observed to be in good agreement. Additionally, the figure also shows that the same set of slip-systems

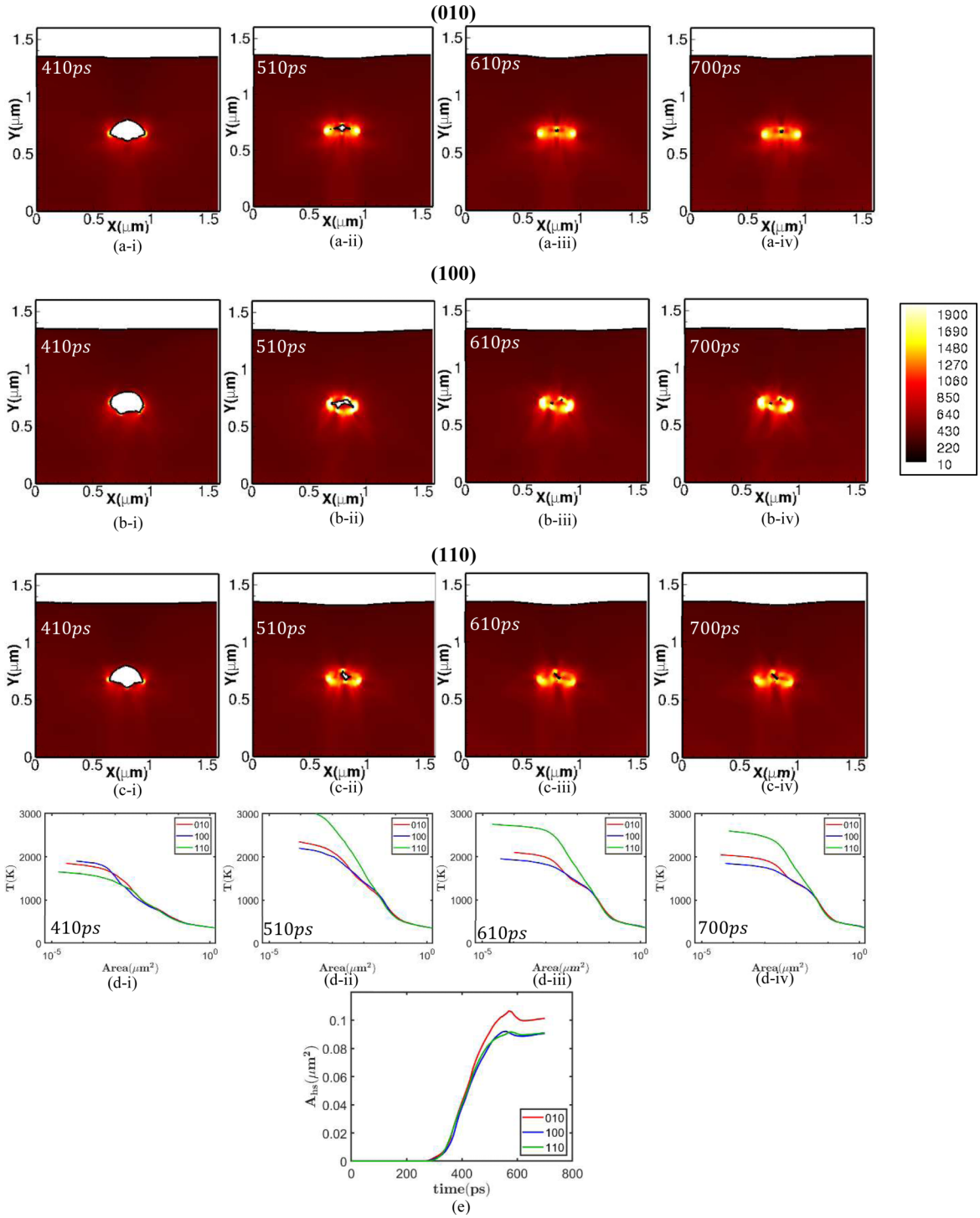

FIG. 13. (a)–(c) Evolution of the temperature field at different instants of time during the collapse of a 0.5 μm void subjected to a velocity of 500 m/s. In Fig. (a), the loading is normal to the (010) plane, while in Figs. (b) and (c), the loading is normal to the (100) and (100) planes, respectively. Figure (d) shows the area with temperature exceeding T at different time instances of void collapse for the three loading directions. Figure (e) shows the variation of the hotspot area, A_{hs}, over time for all three loading directions. A_{hs} is the cumulative area of the material above 650 K.

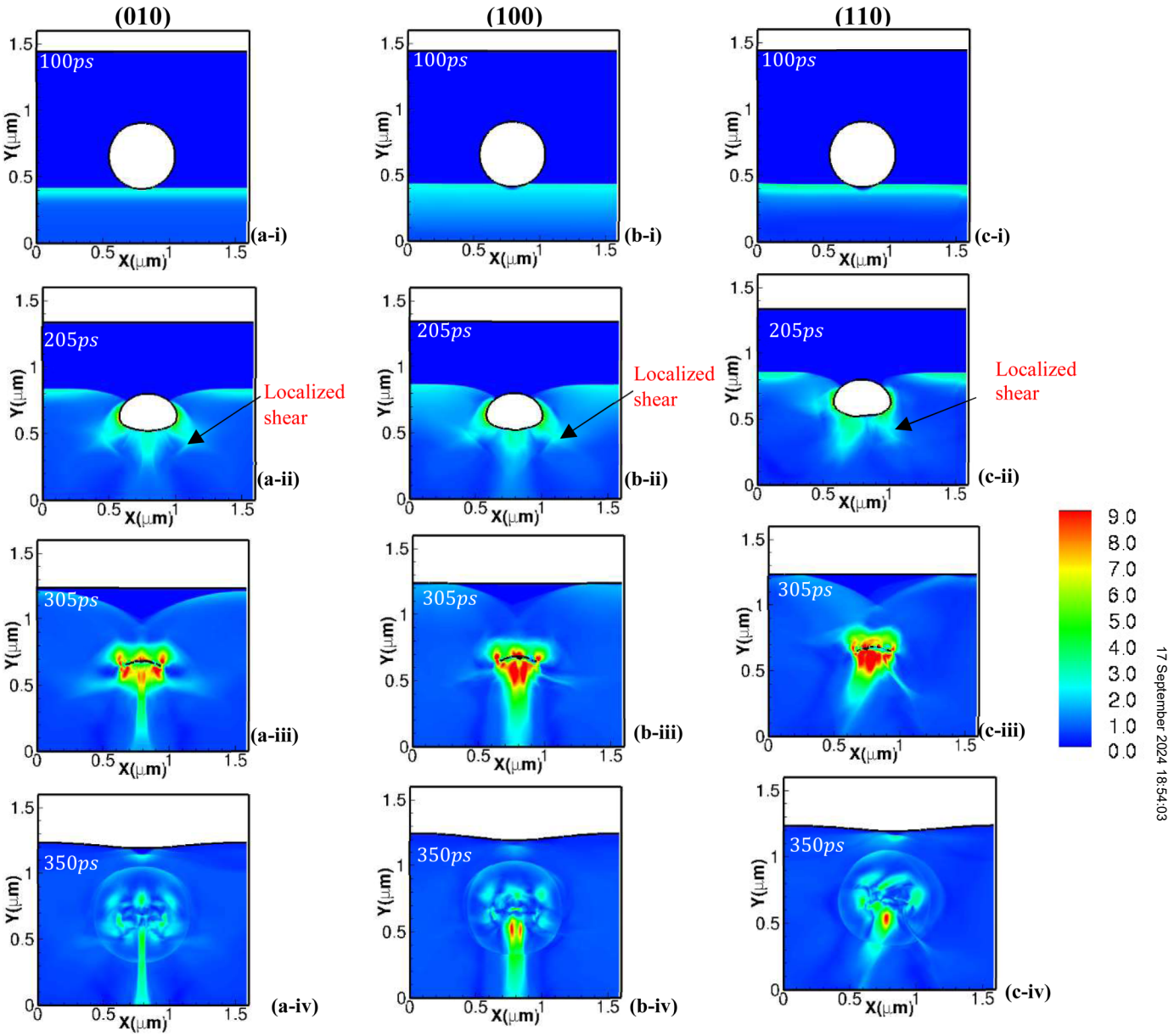

FIG. 14. Evolution of the von Mises stress in GPa at different time-instances during the collapse of a void of diameter 0.5 μm due to a reverse-ballistically induced impact velocity of 1000 m/s. The three columns show the contours of the stress for the shock directed normal to the (100), (010), and (110) planes for HMX. The region of localized shear is indicated in the figures.

are activated in both the formulations for a given loading direction. For instance, Figs. 8(a) and 8(d) show that τ^1 and τ^5 are zero, implying that in both the Eulerian and the Lagrangian computations, all slip-systems, except $\alpha = 1$ and 5 are activated for the (010) direction. Similarly, in the (100) case, the two slip-systems ($\alpha = 1$ and 5) are only weakly activated, as shown in Figs. 9(b) and 9(e). In contrast, for the (110) loading directions, all slip-systems are activated in both the Lagrangian and the Eulerian computations [Figs. 9(c) and 9(f)]. In addition to the activated slip-systems, the Eulerian and the Lagrangian computations also show the same direction of shearing of the slip-systems; τ^8 is seen to be negative for the (010) case, while it is positive for the other two loading directions in Figs. 9(d)–9(f). Therefore, Figs. 8 and 9 show that the Eulerian framework provides reliable and accurate descriptions of

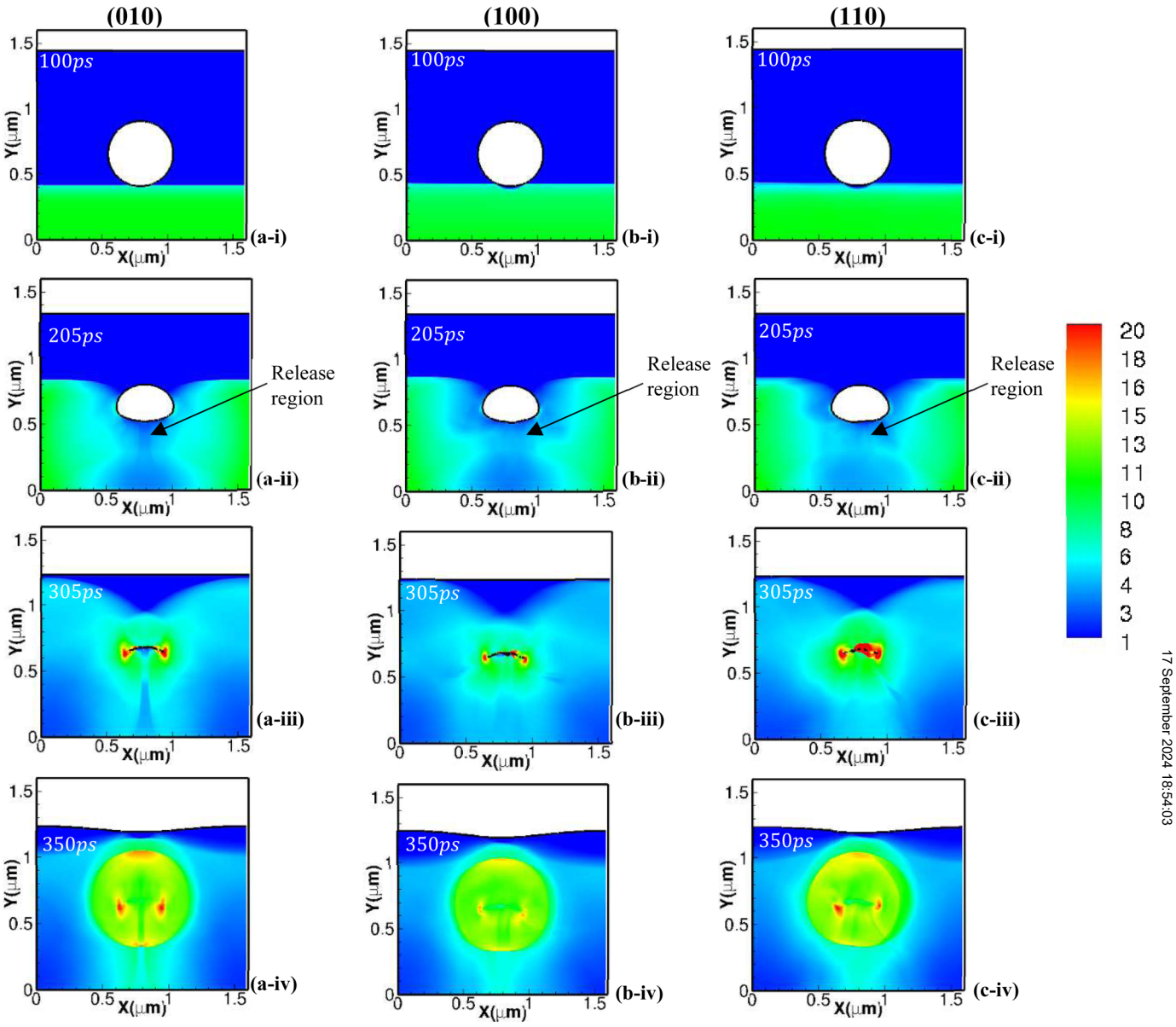

FIG. 15. Evolution of the pressure in GPa at different time-instances during the collapse of a void of diameter 0.5 μm due to a reverse-ballistically induced impact velocity of 1000 m/s. The three columns show the contours of the pressure for the shock directed normal to the (100), (010), and (110) planes for HMX. The release regions are indicated in the figures.

the effects of crystal orientation on the evolution of stresses for materials under shocks.

3. Validation of the elastoplastic computations

While in the previous sections, we compare the current computations with those of a MD-calibrated Lagrangian computational model, here we focus on validating the full elastoplastic Eulerian computational model by comparing with molecular dynamics (MD)[19] and available experimental data.[34] To this end, we load a coupon of β-HMX in the (010) direction in a reverse-ballistic setting, using the computational set-up shown in Fig. 3 (in the absence of a void). The coupon impacts at different particle velocities, viz., $V = 250$, 500, 750, 1000, 1500 , and 2000 m/s and the post-shock pressure, p, as well as the densities, ρ, behind the shock are computed for these velocities. The variation of the calculated

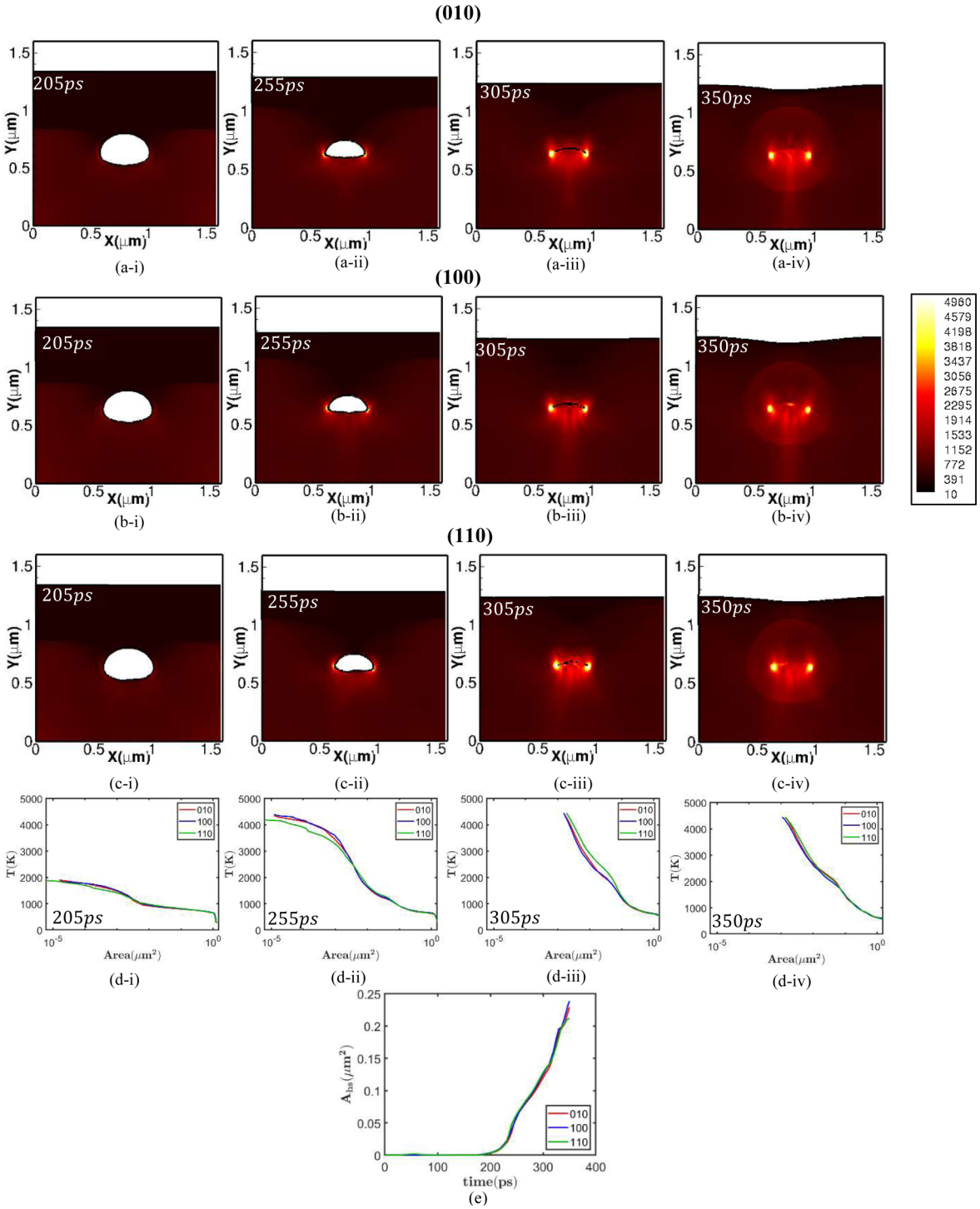

FIG. 16. Evolution of the temperature field at different instants of time during the collapse of a 0.5 μm void subjected to a velocity of 1000 m/s. In Fig. (a), the loading is normal to the (010) plane, while in Figs. (b) and (c), the loading is normal to the (100) and (100) planes, respectively. Figure (d) shows the area with temperature exceeding T at different time instances of void collapse for the three loading directions. Figure (e) shows the variation of the hotspot area, A_{hs}, over time for all three loading directions. A_{hs} is the cumulative area of the material above 1050 K.

post-shock pressure p with the impact velocity U_p is compared with the Hugoniostat data computed using molecular dynamics (MD),[19] while the variation of p with the compression ratio ρ_0/ρ is compared with the experimental Hugoniot curve.[34]

Figure 10(a) compares results from the current Eulerian computations with the MD Hugoniostat data. As observed in the figure, the current computations show excellent agreement with the MD simulations. In particular, it is noted that both in MD as well as in the current Eulerian computations the Hugoniot Elastic Limit (HEL) is observed to be reached at an impact velocity of ≈1 km/s, as discerned from the location on the graph where the slope of the $p - V$ curve shows a discontinuity. In addition to agreement with the MD computations, the computed Hugoniot is also observed to be in good agreement with the experimental Hugoniot[34] in Fig. 10(b). Note that as discussed in Menikoff and Sewell,[34] the experimental Hugoniot data for values of ρ_0/ρ less than 0.65 likely correspond to conditions exceeding the melting point of $\beta - HMX$. Therefore, in the current work, the comparison against the experimental Hugoniot is limited to $V < 2$ km/s, where ρ_0/ρ is greater than 0.65. Therefore, the results in Fig. 10 show that the current Eulerian computations produce good agreement with both MD computations as well as with experiments for the overall elastoplastic shock response of the material.

C. Shock-induced void-collapse in β-HMX

The above validation and benchmarking efforts have demonstrated that the present Eulerian crystal plasticity modeling framework captures the elastoplastic dynamics, including the orientation sensitivity of β-HMX under shock conditions. Initiation sensitivity of shocked HMX-based materials is strongly influenced by the collapse of voids in the material. As shown in the previous work,[11] the sizes of critical voids, i.e., those that lead to critical or self-sustaining hotspots in the energetic material, are centered around 1 μm. Voids of size ranges much smaller or larger than the micron range contribute weakly to the energy localization in β-HMX.[57] To study the collapse of voids relevant to the initiation sensitivity of the material, we study the effect of crystalline anisotropy on the mechanics of void collapse under the conditions of reverse ballistic impact illustrated in Fig. 3. In the computational setup l and w are set to 1.6 and 1.5 μm, respectively. The diameter of the void is taken to be 0.5 μm, which is a representative void-size commonly found in HMX-based explosive formulations.[56] Similar to the previous section, three loading directions are considered: the crystal is orientated such that the impact direction is parallel to the unit normals of the (010), (100), and (110) planes. The evolution of the stresses and temperature in the material for these three loading directions is studied for two impact velocities, viz., $V = 500$ and 1000 m/s as discussed below.

1. Void collapse for impact velocity $V = 500$ m/s

Figures 11 and 12 show the von Mises stress, $\sigma^v = \sqrt{\frac{3}{2}\sigma^d_{ij}\sigma^d_{ij}}$, and the pressure p respectively, at different time instances of void collapse for the low velocity case, $V = 500$ m/s. The columns in each figure show the Mises stresses, at four instants of time through the void collapse process. It can be observed that although the magnitude of p and σ^v are similar for the three loading directions, their distributions differ significantly at a particular instant of time. For instance, in all three cases, the voids begin to collapse at 130 ps, and the maximum values of p and σ^v at the earlier stages of collapse are similar in Figs. 11, 12(a-i), and 12(a-ii). However, while for the (010) direction, a sustained shock impinges on the void, for the other two directions, the void interacts with a shock followed by a release zone. In addition to the initial shock, the rarefaction zones developed during void collapse are also different for the different loading directions. As observed in Figs. 12(a-ii)–12(c-ii), the (010) direction manifests a symmetric rarefaction zone, while the (110) case results in a wider region of expansion.

The differences in the distributions of p and σ^v lead to differences in the shapes of the collapsing voids for the three loading directions. For the (010) direction, Figs. 11 and 12 show that the void collapses symmetrically with respect to its longitudinal axis ($x = 0.75\,\mu$m). For the (100) and the (110) cases on the other hand, Figs. 11 and 12 show that the void shapes are skewed with respect to the longitudinal axis. It is also noted in these figures that the distributions of p and σ^v are symmetric with respect to the longitudinal axis for the (010) case, while this longitudinal symmetry is not observed for the (100) and the (110) directions. Consequently, from Fig. 11, it is noted that there are localized regions of stress in the post-collapse flow field for the (100) and the (110) cases, while such stress localizations are absent in the symmetric flow-field of the (010) case. Figure 13 shows the evolution of the hotspot that results from void collapse for the three loading directions. Similar to the p and σ^v distributions, Figs. 13(a)–13(c) show that the peak temperature in the hotspots is the same for all three loading directions. Furthermore, Figs. 13(a-ii)–13(c-ii) show that in all three cases, the maximum temperature is developed at the edges of the voids, i.e., the hotspots are initiated due to plastic heating as the void is pinched towards closure from the sides; this mode of heating and collapse is distinctly different from the hydrodynamic jetting mode, which is commonly observed for isotropic, elastic-perfectly plastic models of β-HMX.[11] However, while the orientation of the crystal has modest effects on the maximum temperatures or the mode of hotspot formation (i.e., pinching from the sides as opposed to jetting from the lower surface), the distribution of the temperatures is significantly affected by the crystal orientation. Thus, Fig. 13(a) shows that the hotspots are formed as two distinct circular lobes of high temperature which are symmetric with respect to the longitudinal axis of the void for the (010) case. In contrast, for the (100) case, the hotspots originate as annular regions of high-temperature [for example, at 510 ps, Fig. 13(b-ii)] and the post-collapse hotspot is asymmetric with respect to the longitudinal axis. The (110) case also shows asymmetric hotspots [Fig. 13(c)]; however, instead of circular lobes or annular structures, the hotspots evolve as convex regions of high temperature.

Hotspot areas formed due to void collapse are known to depend on the void size, shock strength, and on the porosity of the material. The hotspot areas are also expected to depend on the crystalline orientations; we examine this orientational dependency in Fig. 13. Figure 13(d) shows the area occupied by regions at the specified cumulative temperature at different instances of time. From the figure, it is observed that the local temperatures for the (110) case are initially lower [e.g., at 410 ps in Fig. 13 (d-i)], while

at later times, they are lower for the (010) and the (100) cases. Finally, Fig. 13(e) shows the temporal variation of the total area of the hotspot, A_{hs}, which is calculated to be the cumulative area of the domain at a temperature $T > 650$ K. The figure shows that A_{hs} is slightly higher for the (010) case, i.e., where the hotspots develop as circular lobes, compared to the other loading directions. Thus, crystalline anisotropy has observable effects on the shapes of hotspots developed during shock-induced void-collapse.

2. Void collapse at $V = 1000$ m/s

Figures 14 and 15 show the distributions of σ^v and p at different time instances during void collapse under a higher shock strength, corresponding to a velocity $V = 1000$ m/s. Unlike for $V = 500$ m/s, the figures show only modest effects of loading directions on the distributions of σ^v and p for $V = 1000$ m/s. Thus, Figs. 14, 15(a), and 15(b) show that the distributions of σ^v and p are symmetric with respect to the longitudinal axis ($x = 0.75\,\mu$m) for the (010) and the (100) cases, while only minor asymmetries are noted for the (110) case in Figs. 14 and 15(c). Furthermore, in contrast to the $V = 500$ m/s cases where the void collapsed due to pinching from the sides, for $V = 1000$ m/s, the mode of collapse is noted to be predominantly hydrodynamic jetting for all three directions. As seen in Figs. 14 and 15, the lower surface of the impinges on the opposite surface in a typical jet formation. Finally, yet another difference between the $V = 500$ and $V = 1000$ m/s cases is that a distinct post-collapse spherical blast wave is observed at 350 ps for the latter case. The figures also show complex interactions of the blast-wave with localized zones of σ^v and p concentrations in all three loading directions. These are markers of a hydrodynamics dominated deformation and void collapse process.

All of the aforementioned differences between the $V = 500$ m/s cases and $V = 1000$ m/s indicate that for the higher velocity case, pressure predominates over the deviatoric stresses during void collapse. Since the equation of state [Eqs. (5) and (6)] is isotropic, despite the anisotropic models for the isochoric deformations, loading directions only modestly affect the distribution of σ^v and p. However, the anisotropic material models are observed to influence the σ^v localizations in the core of collapse in Fig. 14. In fact, localized zones of high σ^v concentrations are observed for the (010) and the (010) cases at 205 ps in Fig. 14; these localized zones manifest as sharp lines intersecting with a crisscross pattern, e.g., at $x = 0.5$ and $1.25\,\mu$m and $y = 0.5\,\mu$m. As the flow evolves, these localized regions of high σ^v develop further with time and manifest as isolated bands emanating from the core of collapse in the figure. A single band is also observed to develop for the (110) case in Fig. 14. However, unlike the (010) and (100) cases, this band does not develop symmetrically with respect to the longitudinal axis. It is expected that thermal softening of the plastic strain would localize the bands further and result in distinct shear-bands or melt-cracks, as has been observed previously by Austin et *al.*[3] as well as others[33,61,62] for isotropic rate dependent elastoplasticity models used for simulating void collapse. Models for such thermal softening and localization are available for crystal plasticity material descriptions of organic crystals[3,6,10,17] and will be studied in future work.

Figure 16 shows the evolution of hotspots during void-collapse for $V = 1000$ m/s. Figures (a) through (c) show that for all three loading directions, the hotspots originate as circular lobes of regions of high temperature at the edge of the collapsed voids. This is in contrast to the $V = 500$ m/s cases, where it was observed that for the (100) and (110) cases the hotspots developed as annular and convex regions, respectively, while distinct circular lobes were observed only for the (010) case. Furthermore, contrary to the $V = 500$ m/s, Figs. 16(a)–16(c) show that the hotspots are symmetric with respect to the longitudinal axis for $V = 1000$ m/s. Additionally, Figs. 16(d) and 16(e) show the local temperature distributions and the hotspot area (defined as the cumulative area under a temperature above 1050 K, which is approximately the bulk temperature in a void-free material subjected to an impact velocity of 1000 m/s). The evolution of the local temperature and hotspot area is virtually indistinguishable for the three loading directions. Thus, similar to σ^v and p, for this high velocity case of $V = 1000$ m/s, the temperature field is also nearly unaffected by anisotropy, i.e., the hotspot evolution is largely governed by the isotropic equation of state for the pressure. Thus, the regime of impact velocity/shock strength where crystalline anisotropy plays a role in the void collapse behavior of β-HMX is limited to velocities significantly lower than 1000 m/s.

IV. CONCLUSIONS

This paper presented a Eulerian framework for computational modeling of anisotropic elastoplastic response of crystalline materials under shocks and high-strain rate loading conditions. The framework was used to compute the shock response of a monoclinic high-explosive material, β-HMX. It was shown that the results from the Eulerian framework agreed well with those of Lagrangian computations. For an initially planar shock, the volumetric and deviatoric stresses from the Eulerian and the Lagrangian computations were in close agreement with each other for three different loading directions for both a purely elastic as well as a full elastoviscoplastic material model. Good agreement was also shown for the individual resolved shear stresses along specific slip systems activated during shock loading for different crystalline orientations relative to the shock direction. Differences in stress distributions between the Eulerian and Lagrangian simulations were due to the use of artificial viscosity in the finite element Lagrangian framework. Such artificial viscosity is not required in the Eulerian framework due to the inbuilt entropy satisfying condition in the shock-capturing (ENO) scheme employed. After establishing confidence in the Eulerian calculations, the framework was validated against Hugoniostat data obtained from molecular dynamics calculations as well as experimental data for the full elastoplastic material model. It was shown that the current Eulerian framework accurately predicts the shock Hugoniot of β-HMX.

The framework developed was then used to simulate collapse of a $0.5\,\mu$m isolated void in β-HMX under two different loading velocities to study the effect of anisotropy and loading direction on hotspots. For the lower loading velocity, viz., $V = 500$ m/s, the distributions of the von Mises stresses and the pressure as well as the hotspot shapes were affected significantly by the loading direction and material anisotropy. On the other hand, for higher impact

velocity of $V = 1000$ m/s, the collapse was predominantly in the form of hydrodynamic jetting. Therefore, the pressure obtained from the isotropic equation of state dominates over the deviatoric stresses from the anisotropic isochoric constitutive laws; rather weak effects of loading directions on the von Mises stresses, pressure, and temperature distributions were observed for the high impact velocity.

Several extensions of the Eulerian framework are currently under way. First, more advanced single crystal viscoplastic models with thermal softening of the material are being incorporated. This will allow for shear-induced localization under shock loading, culminating in the development of shear bands in the material. Such shear bands can serve as additional sources of hotspots and initiation in the material under moderate shock loads. Second, high-order numerical schemes and local mesh refinement are being deployed to better resolve the evolution equations of the subgrid-scale lattice variables. Finally, reactive void-collapse simulations employing anisotropic constitutive models are being performed to study the effects of crystalline orientations on hotspot ignition and growth rates. These extensions will enable greater physical fidelity in calculating various sources of energy localization (and their interactions), leading to accurate, anisotropy-sensitive models of initiation in energetic materials.

ACKNOWLEDGMENTS

Research was sponsored by the Army Research Laboratory and was accomplished under Cooperative Agreement No. W911NF-19-2-0110. The views and conclusions contained in this document are those of the authors and should not be interpreted as representing the official policies, either expressed or implied, of the Army Research Laboratory or the U.S. Government. The U.S. Government is authorized to reproduce and distribute reprints for Government purposes notwithstanding any copyright notation herein. We also gratefully acknowledge support from an AFOSR-MURI Grant (No. FA9550-19-1-0318). The work of C.A.D. and M.K. was supported by the U.S. Department of Defense, Office of Naval Research, MURI Contract No. N00014-16-1-2557. The authors would like to thank Drs. Catalin Picu (Rensselaer Polytechnic Institute), Tommy Sewell (University of Missouri, Columbia), Amit Acharya (Carnegie Mellon University), D. J. Luscher (Los Alamos National Laboratory), and Jia Lu (University of Iowa) for their insights and discussions while developing the Eulerian framework for crystal plasticity.

AUTHOR DECLARATIONS

Conflict of Interest

The authors have no conflicts to disclose.

Author Contributions

Oishik Sen: Conceptualization (equal); Investigation (equal); Methodology (equal); Writing – original draft (equal); Writing – review & editing (equal). **Camilo A. Duarte:** Conceptualization (equal); Formal analysis (equal). **Nirmal Kumar Rai:** Conceptualization (equal); Methodology (equal). **Marisol Koslowski:** Conceptualization (equal); Writing – review & editing (equal). **H. S. Udaykumar:** Conceptualization (equal); Validation (equal); Writing – original draft (equal); Writing – review & editing (equal).

DATA AVAILABILITY

The data that support the findings of this study are available from the corresponding author upon reasonable request.

REFERENCES

[1]N. K. Rai and H. S. Udaykumar, "Three-dimensional simulations of void collapse in energetic materials," Phys. Rev. Fluids **3**, 033201 (2018).
[2]H. K. Springer, S. Bastea, A. L. Nichols, III, C. M. Tarver, and J. E. Reaugh, "Modeling the effects of shock pressure and pore morphology on hot spot mechanisms in HMX," Propellants, Explos., Pyrotech. **43**, 805–817 (2018).
[3]R. A. Austin, N. R. Barton, J. E. Reaugh, and L. E. Fried, "Direct numerical simulation of shear localization and decomposition reactions in shock-loaded HMX crystal," J. Appl. Phys. **117**, 185902 (2015).
[4]K. Ding, X.-J. Wang, Z.-P. Duan, Y.-Q. Wu, and F.-L. Huang, *Shock Response of Cyclotetramethylene Tetranitramine (HMX) Single Crystal at Elevated Temperatures* (Defence Technology, 2021).
[5]N. Grilli and M. Koslowski, "The effect of crystal orientation on shock loading of single crystal energetic materials," Comput. Mater. Sci. **155**, 235–245 (2018).
[6]N. R. Barton, N. W. Winter, and J. E. Reaugh, "Defect evolution and pore collapse in crystalline energetic materials," Modell. Simul. Mater. Sci. Eng. **17**, 035003 (2009).
[7]S. Roy, B. P. Johnson, X. Zhou, Y. T. Nguyen, D. D. Dlott, and H. Udaykumar, "Hot spot ignition and growth from tandem micro-scale simulations and experiments on plastic-bonded explosives," J. Appl. Phys. **131**, 205901 (2022).
[8]M. Adler, J. West, S. Lele, "High-order methods for plastic deformation in multi-material Richtmyer-Meshkov instabilities," in APS Division of Fluid Dynamics Meeting Abstracts (American Physical Society, 2020), p. Z09.005.
[9]N. S. Ghaisas, A. Subramaniam, and S. K. Lele, "A unified high-order Eulerian method for continuum simulations of fluid flow and of elastic–plastic deformations in solids," J. Comput. Phys. **371**, 452–482 (2018).
[10]D. J. Luscher, F. L. Addessio, M. J. Cawkwell, and K. J. Ramos, "A dislocation density-based continuum model of the anisotropic shock response of single crystal α-cyclotrimethylene trinitramine," J. Mech. Phys. Solids **98**, 63–86 (2017).
[11]N. K. Rai and H. S. Udaykumar, "Void collapse generated meso-scale energy localization in shocked energetic materials: Non-dimensional parameters, regimes, and criticality of hotspots," Phys. Fluids **31**, 016103 (2019).
[12]W. Noh and M. Protter, "Difference methods and the equations of hydrodynamics," J. Math. Mech. **12**, 149–191 (1963).
[13]H. Fan, Y. Long, L. Ding, J. Chen, and F.-D. Nie, "A theoretical study of elastic anisotropy and thermal conductivity for TATB under pressure," Comput. Mater. Sci. **131**, 321–332 (2017).
[14]M. Khan, A. Pal, and C. R. Picu, "Dislocation mobility and critical stresses at finite temperatures in molecular crystal cyclotetramethylene tetranitramine (β-HMX)," Modell. Simul. Mater. Sci. Eng. **26**, 085009 (2018).
[15]M. Khan and C. R. Picu, "Dislocation cross slip in molecular crystal cyclotetramethylene tetranitramine (β-HMX)," J. Appl. Phys. **126**, 155105 (2019).
[16]A. Pal and C. R. Picu, "Non-Schmid effect of pressure on plastic deformation in molecular crystal HMX," J. Appl. Phys. **125**, 215111 (2019).
[17]R. A. Austin and D. L. McDowell, "Parameterization of a rate-dependent model of shock-induced plasticity for copper, nickel, and aluminum," Int. J. Plast. **32–33**, 134–154 (2012).
[18]C. A. Duarte, A. Hamed, J. D. Drake, C. J. Sorensen, S. F. Son, W. W. Chen, and M. Koslowski, "Void collapse in shocked-HMX single crystals: Simulations and experiments," Propellants, Explos., Pyrotech. **45**, 243–253 (2020).
[19]C. A. Duarte, C. Li, B. W. Hamilton, A. Strachan, and M. Koslowski, "Continuum and molecular dynamics simulations of pore collapse in shocked

β-tetramethylene tetranitramine (β-HMX) single crystals," J. Appl. Phys. **129**, 015904 (2021).
[20]A. De Brauer, N. K. Rai, M. E. Nixon, and H. S. Udaykumar, "Modeling impact-induced damage and debonding using level sets in a sharp interface Eulerian framework," Int. J. Numer. Methods Eng. **115**, 1108–1137 (2018).
[21]A. Kapahi, S. Sambasivan, and H. S. Udaykumar, "A three-dimensional sharp interface Cartesian grid method for solving high speed multi-material impact, penetration and fragmentation problems," J. Comput. Phys. **241**, 308–332 (2013).
[22]L. B. Tran and H. S. Udaykumar, "A particle-level set-based sharp interface cartesian grid method for impact, penetration, and void collapse," J. Comput. Phys. **193**, 469–510 (2004).
[23]A. Kapahi, J. Mousel, S. Sambasivan, and H. S. Udaykumar, "Parallel, sharp interface Eulerian approach to high-speed multi-material flows," Comput. Fluids **83**, 144–156 (2013).
[24]D. J. Benson, "Computational methods in Lagrangian and Eulerian hydrocodes," Comput. Methods Appl. Mech. Eng. **99**, 235–394 (1992).
[25]M. Nikodemou, L. Michael, and N. Nikiforakis, "A unified multi-phase and multi-material formulation for combustion modeling," Phys. Fluids **33**, 106113 (2021).
[26]J. B. Bdzil, R. Menikoff, S. F. Son, A. K. Kapila, and D. S. Stewart, "Two-phase modeling of deflagration-to-detonation transition in granular materials: A critical examination of modeling issues," Phys. Fluids **11**, 378–402 (1999).
[27]N. K. Rai, S. P. Koundinyan, O. Sen, I. V. Schweigert, B. F. Henson, and H. S. Udaykumar, "Evaluation of reaction kinetics models for meso-scale simulations of hotspot initiation and growth in HMX," Combust. Flame **219**, 225–241 (2020).
[28]R. C. Roberts, Methods in Computational Physics. Volume 3 Fundamental Methods in Hydrodynamics (JSTOR, 1966).
[29]M. A. Meyers, *Dynamic Behavior of Materials* (John Wiley & Sons, 1994).
[30]O. Cazacu and I. R. Ionescu, "Dynamic crystal plasticity: An Eulerian approach," J. Mech. Phys. Solids **58**, 844–859 (2010).
[31]J. Kratochvíl, J. Málek, and P. Minakowski, "A Gibbs-potential-based framework for ideal plasticity of crystalline solids treated as a material flow through an adjustable crystal lattice space and its application to three-dimensional micropillar compression," Int. J. Plast. **87**, 114–129 (2016).
[32]S. K. Sambasivan and H. S. UdayKumar, "Ghost fluid method for strong shock interactions. Part 2: Immersed solid boundaries," AIAA J. **47**, 2923–2937 (2009).
[33]N. K. Rai, E. M. Escauriza, D. E. Eakins, and H. Udaykumar, "Mechanics of shock induced pore collapse in poly (methyl methacrylate)(PMMA): Comparison of simulations and experiments," J. Mech. Phys. Solids **143**, 104075 (2020).
[34]R. Menikoff and T. D. Sewell, "Constituent properties of HMX needed for mesoscale simulations," Combust. Theory Modell. **6**, 103–125 (2002).
[35]A. Kapahi and H. S. Udaykumar, "Dynamics of void collapse in shocked energetic materials: Physics of void–void interactions," Shock Waves **23**, 537–558 (2013).
[36]B. J. Plohr and D. H. Sharp, "A conservative formulation for plasticity," Adv. Appl. Math. **13**, 462–493 (1992).
[37]N. Favrie, S. Gavrilyuk, and S. Ndanou, "A thermodynamically compatible splitting procedure in hyperelasticity," J. Comput. Phys. **270**, 300–324 (2014).
[38]D. L. Hastings and E. L. Dreizin, "Reactive structural materials: Preparation and characterization," Adv. Eng. Mater. **20**, 1700631 (2018).
[39]T. Brepols, I. N. Vladimirov, and S. Reese, "Numerical comparison of isotropic hypo-and hyperelastic-based plasticity models with application to industrial forming processes," Int. J. Plast. **63**, 18–48 (2014).
[40]H.-C. Wu, *Continuum Mechanics and Plasticity* (CRC Press, 2004).
[41]O. T. Bruhns, "The Prandtl-Reuss equations revisited," ZAMM-J. Appl. Math. Mech./Z. Angew. Math. Mech. **94**, 187–202 (2014).
[42]M. A. Slawinski, *Waves and Rays in Elastic Continua* (World Scientific, 2010).
[43]S. Nemat-Nasser, *Plasticity: A Treatise on Finite Deformation of Heterogeneous Inelastic Materials* (Cambridge University Press, 2004).
[44]D. Peirce, R. J. Asaro, and A. Needleman, "Material rate dependence and localized deformation in crystalline solids," Acta Metall. **31**, 1951–1976 (1983).
[45]S. R. Kalidindi and L. Anand, "An approximate procedure for predicting the evolution of crystallographic texture in bulk deformation processing of fcc metals," Int. J. Mech. Sci. **34**, 309–329 (1992).
[46]C. J. Permann, D. R. Gaston, D. Andrš, R. W. Carlsen, F. Kong, A. D. Lindsay, J. M. Miller, J. W. Peterson, A. E. Slaughter, and R. H. Stogner, "MOOSE: Enabling massively parallel multiphysics simulation," SoftwareX **11**, 100430 (2020).
[47]C.-W. Shu, "Essentially non-oscillatory and weighted essentially non-oscillatory schemes for hyperbolic conservation laws," in *Advanced Numerical Approximation of Nonlinear Hyperbolic Equations* (Springer, 1998), pp. 325–432.
[48]E. F. Toro, *Riemann Solvers and Numerical Methods for Fluid Dynamics: A Practical Introduction* (Springer Science & Business Media, 2013).
[49]Q. Du, R. Glowinski, M. Hintermüller, and E. Süli, *Handbook of Numerical Methods for Hyperbolic Problems: Basic and Fundamental Issues* (Elsevier, 2016).
[50]S. C. Chapra and R. P. Canale, *Numerical Methods for Engineers* (McGraw-Hill, New York, 2011).
[51]H. N. Najm, C. Safta, J. Ortega, M. Valorani, D. Goussis, and M. Frenklach, *Adaptive Explicit Integration of Stiff Chemical Systems* [Sandia National Lab. (SNL-CA), Livermore, CA, 2007].
[52]J. A. Sethian, "A fast marching level set method for monotonically advancing fronts," Proc. Natl. Acad. Sci. U.S.A. **93**, 1591–1595 (1996).
[53]R. P. Fedkiw, T. Aslam, B. Merriman, and S. Osher, "A non-oscillatory Eulerian approach to interfaces in multimaterial flows (the ghost fluid method)," J. Comput. Phys. **152**, 457–492 (1999).
[54]P. Das, O. Sen, G. Jacobs, and H. S. Udaykumar, "A sharp interface Cartesian grid method for viscous simulation of shocked particle-laden flows," Int. J. Comput. Fluid Dyn. **31**, 269–291 (2017).
[55]J. Massoni, R. Saurel, A. Lefrancois, and G. Baudin, "Modeling spherical explosions with aluminized energetic materials," Shock Waves **16**, 75–92 (2006).
[56]S. Roy, O. Sen, N. Rai, M. Moon, E. Welle, C. Molek, K. Choi, and H. Udaykumar, "Structure–property–performance linkages for heterogenous energetic materials through multi-scale modeling, multiscale and multidisciplinary modeling," Exp. Des. **3**, 265–293 (2020).
[57]C. A. Handley, B. D. Lambourn, N. J. Whitworth, H. R. James, and W. J. Belfield, "Understanding the shock and detonation response of high explosives at the continuum and meso scales," Appl. Phys. Rev. **5**, 011303 (2018).
[58]A. Nassar, N. K. Rai, O. Sen, and H. Udaykumar, "Modeling mesoscale energy localization in shocked HMX, part I: Machine-learned surrogate models for the effects of loading and void sizes," Shock Waves **29**, 537–558 (2019).
[59]W. F. Noh, "Errors for calculations of strong shocks using an artificial viscosity and an artificial heat flux," J. Comput. Phys. **72**, 78–120 (1987).
[60]A. E. Mattsson and W. J. Rider, "Artificial viscosity: Back to the basics," Int. J. Numer. Methods Fluids **77**, 400–417 (2015).
[61]H. K. Springer, J. Gambino, S. Bastea, A. Nichols, and C. Tarver, "Hot spot criticality in shocked HMX over a range of pore sizes and pressures," AIP Conf. Proc. **2272**, 070044(2020).
[62]P. Das, P. Zhao, D. Perera, T. Sewell, and H. S. Udaykumar, "Molecular dynamics-guided material model for the simulation of shock-induced pore collapse in β-octahydro-1, 3, 5, 7-tetranitro-1, 3, 5, 7-tetrazocine (β-HMX)," J. Appl. Phys. **130**, 085901 (2021).